Title:

Inferring Long-Term Tectonic Uplift Patterns from Bayesian Inversion of Fluvially-Incised Landscapes

Bar Oryan[1*], Boris Gailleton[2], Jean-Arthur Olive[3], Luca C. Malatesta[4] and Romain Jolivet[3,5]

Affiliations:

(1)Scripps Institution of Oceanography, UC San Diego, La Jolla, CA 92093,USA

(2)Univ. Rennes, Géosciences Rennes, UMR 6118, 35000 Rennes, France.

(3)Laboratoire de Géologie, École normale supérieure – PSL, CNRS UMR 8538, Paris, France.

(4)Earth Surface Process Modelling, GFZ German Research Center for Geosciences, Potsdam, Germany.

(5)Institut Universitaire de France, 1 rue Descartes, 75006 Paris.

Corresponding author email:

Bar Oryan - Bar.oryan@columbia.edu

Abstract

Earth surface processes encode the combined forcing of tectonics and climate in topography. Separating their contributions is essential for using landscapes as quantitative records of crustal deformation. Here, we develop a method for inverting fields of long-term rock uplift from fluvially-incised landscapes, while accounting for spatial variability in climatic conditions and rock erodibility. Our approach operates in the χ-space reference frame and handles spatial variability in key geomorphological parameters using B-spline interpolating functions. Through inversions of 170 synthetic landscapes, we demonstrate that our method accurately captures spatial variations in landscape properties, even when applied to settings that deviate from the ideal model of equilibrated detachment-limited channels, which underpins the χ-space framework. Consequently, we apply our inversion to five natural landscapes shaped by normal faults (half-grabens), and to a 200 km wide region of the Himalayas. We show that our inversion can resolve the effect of climate and lithology while extracting uplift fields that are consistent with patterns expected from upper crustal flexure and previous estimates of uplift derived from geomorphological markers. The success of our method in recovering uplift patterns, isolated from the effects of climate and erodibility, highlights its applicability to settings where long-term uplift trends are unknown, paving the path to deciphering time-averaged tectonic fingerprints recorded in landscapes over tens of thousands of years.

Plain Language Summary

Earth's topography is uniquely shaped by both deep tectonic activity and the erosive processes that sculpt its surface. Utilizing these landscapes to deduce tectonic activity presents valuable insights, albeit elusive. In this study, we introduce a mathematical inversion method utilizing geomorphic indices to extract tectonic uplift patterns from landscapes. We assess this method's effectiveness on simulated synthetic landscapes that include a variety of surface processes. Our findings confirm that the method can accurately retrieve uplift rate patterns, even in landscapes not solely governed by steady state detachment-limited erosion—the assumption underlying our inversion technique. Applying this method to natural landscapes shaped by normal faults and the Himalayas, we demonstrate that our extracted uplift patterns align with expected patterns of tectonic warping. This approach sets the stage for using landscapes to decipher tectonic signals accumulated over tens of thousands of years.

Key Points

- New method infers unknown uplift patterns and variable erodibility from fluvial landscapes using a Bayesian approach.
- Synthetic tests reveal the broad applicability of our methods, even in systems that deviate from the steady-state detachment-limited incision assumption.
- Inverting six natural landscapes yields uplift fields consistent with previous uplift estimates and crustal flexure.

1 Introduction

Earth's topography reflects a delicate balance between internal tectonic forcings and climate-modulated surface processes. The first induce vertical motion of the surface through processes such as faulting, dynamic topography and isostasy (e.g., Faccenna et al., 2019; King et al., 1988; Watts, 2001) while the latter level relief by eroding bedrock and transporting/ depositing the resulting sediments (e.g., Merritt et al., 2003). Thus, the shape of landscapes represents a snapshot of the ever-evolving competition of these two processes (Kirby & Whipple, 2012; Molnar & England, 1990; Willgoose et al., 1991).

Disentangling the contributions of surface processes and tectonic forces is crucial for deriving insights into tectonic activities, which is a core goal of tectonic geomorphology (e.g., Armijo et al., 1996; Lavé & Avouac, 2001; Malatesta et al., 2021). Extracting spatial patterns of rock uplift rates from landscapes is particularly important as it provides direct quantitative constraints on the underlying tectonic mechanisms. For instance, in landscapes shaped by normal faults, spatially-varying vertical rock uplift are used to estimate the effective elastic thickness of the lithosphere (Armijo et al., 1996). The shape of uplift recorded around fault scarps offers insights into the slip behavior of the fault (e.g, Holtmann et al., 2023). Perhaps even more critically, variations in rock uplift rates across subduction zone forearcs may be used to infer the pattern of interseismic locking on the megathrust. This is because the latter modulates the accumulation of inelastic strain over multiple seismic cycles, which is ultimately encoded in forearc landscapes (e.g., Cattin & Avouac, 2000; Jolivet et al., 2020; Malatesta et al., 2021; Meade, 2010; Oryan et al., 2024; Dublanchet & Olive, 2024) .

Nonetheless, extracting uplift fields from landscapes is challenging especially in the absence of thermochronological data or geomorphological markers. Current approaches (Castillo et al., 2014; Densmore et al., 2007; Ponza et al., 2010; Su et al., 2017) rely on the stream power incision model (Howard & Kirby, 1983) utilizing a landscape metric called the steepness index, k_{sn} (Wobus et al., 2006, See section 2 for definition). While useful, k_{sn} expresses the ratio of rock erodibility to rock uplift and may be strongly skewed by unconstrained spatial variations in rock erodibility. Furthermore, it depends on point measurements of surface slopes, which can be noisy (Boris Gailleton et al., 2021). The χ metric, which integrates upstream changes in drainage area normalized by the concavity index across entire river networks, provides a quantitative alternative to recover spatial variations in uplift rates from landscapes (Perron & Royden, 2013). Previous work has employed the χ metric for landscape inversion focusing on uplift rate history, while neglecting or prescribing variations in uplift shape (Croissant & Braun, 2014; Fox et al., 2014; L. Goren et al., 2014; Liran Goren et al., 2022; Pritchard et al., 2009; Smith et al., 2024).

Here we extend the χ coordinate framework and invert landscapes for an unknown (steady) field of rock uplift rate and variable spatial erodibility. To that end, we utilize a Bayesian quasi-Newton inversion scheme which optimizes uplift shapes parameterized by B-spline interpolation functions in a manner that minimizes the misfit between measured and inverted elevation. We test the strengths and limitations of our method using synthetic landscapes and demonstrate its ability to recover uplift shapes and erodibility coefficients while accounting for climatic effects. Subsequently, we apply our method to six natural landscapes shaped by divergent and convergent tectonics to demonstrate its effectiveness in real-world scenarios.

2 Inferring tectonic uplift from landscapes within the stream power framework

2.1 The detachment-limited stream power model

The stream power incision model posits that the erosion rate of a riverbed at a certain point is linked to water flux (captured by proxy with drainage area A), channel slope ($\frac{dz}{dx}$) and the erodibility of the material (K) (Hack, 1973; Howard & Kerby, 1983). To maintain a uniform rate of erosion, the river gradient diminishes downstream as drainage area increases, resulting in a familiar concave river profile. According to this model, the change in elevation over time t, of a river eroding at rate, E, under rock uplift, U, is described as follows:

$$1.\quad \frac{\partial z(x,y,t)}{\partial t} = U(x,y,t) - E(x,y,t) = U(x,y,t) - K(x,y,t)A(x,y,t)^m\left(\frac{\partial z}{\partial x}\right)^n$$

Where *m* and *n* are constants, *(x,y)* is position, hereafter denoted as $\vec{x}$ for concision. The velocity at which a change in uplift rate travels upstream as a knickpoint is linked to local erodibility, drainage area and topographic gradient (Rosenbloom & Anderson, 1994; Whipple & Tucker, 1999):

$$2.\quad c(\vec{x}) = k(\vec{x})A(\vec{x})\left(\frac{dz(\vec{x})}{dx}\right)^{n-1}$$

The time for a perturbation to travel from the river base upstream to point x_s is defined as follows (Whipple & Tucker, 1999):

$$3.\quad \tau(x_s) = \int_0^{x_s}\frac{dx}{c(\vec{x})} = \int_0^{x_s}\frac{dx}{k(\vec{x})A(\vec{x})\left(\frac{dz(\vec{x})}{dx}\right)^{n-1}}$$

When erosion and uplift rates are balanced, the steady-state equation describes the equilibrium slope of the river with an inverse power-law relationship between channel slope and drainage area:

$$4.\quad \frac{dz}{dx} = k_{sn}A(\vec{x})^{-\frac{m}{n}}$$

Where $k_{sn} = \left(\frac{U(\vec{x})}{K(\vec{x})}\right)^{\frac{1}{n}}$ a quantity often normalized with respect to regional concavity value, $\theta\_ref(=\frac{m}{n})$ and introduced as k_{sn} which is used as a proxy of uplift to erosion ratio.

2.2 The integral approach: river profiles in χ-space

Upstream integration of equation 4 from an arbitrary base level x_b results in (Perron & Royden, 2013):

$$5.\quad z(\vec{x}) = z(x_b) + a_s \cdot \chi(\vec{x})$$

Where,

$$6.\quad \chi = \int_{x_b}^{x} \frac{dx}{A^*(\vec{x})^{\frac{m}{n}}}\,;\, a_s = \left(\frac{U_0}{K_0 A_o^m}\right)^{\frac{1}{n}}$$

and A_o is a constant reference drainage area such that $A^*(x) = \frac{A(x)}{A_0}$ is dimensionless. The integral along x here denotes an upstream path a connected network of tributaries.

This coordinate transformation allows us to describe river profiles in terms of χ and z. In the case of spatially uniform *U* and *K*, stream profiles in χ -space will exhibit a linear relationship between the two variables, characterized by a slope a_S. In landscapes where erodibility and uplift vary spatially , the definition of χ can be amended as (Olive et al., 2022; Perron & Royden, 2013) :

$$7.\quad \chi_{u,k} = \int_{x_b}^{x} \left(\frac{U^*(\vec{x})}{A^*(\vec{x})^m K^*(\vec{x})}\right)^{\frac{1}{n}} dx\,;\, a_s = \left(\frac{U_o}{K_o A_o^m}\right)^{\frac{1}{n}}$$

In this case, U_0 and K_0 are reference values so the trailing terms are dimensionless ($U^* = \frac{U}{U_0}$, $K^* = \frac{K}{K_0}$). $\chi_{u,k}$ denotes a version of χ corrected for known spatial variations in uplift rate and erodibility. If $U^*(\vec{x})$ and $K^*(\vec{x})$ are properly accounted for, the steady state landscape should verify equation (5): elevation should be linearly correlated with $\chi_{u,k}$.

3 Inverting uplift shapes from river incised landscapes

3.1 Forward model

3.1.1 Parameter space, data space and cost function

The detachment-limited stream power model in χ-space provides a robust framework to invert uplift shape from river incised landscapes. Let us begin by outlining the direct (forward) problem of river profiles in χ-space, from knowledge of the parameters $m, n, a_s, U^*(\vec{x})$ and $K^*(\vec{x})$. This is done by computing $\chi_{u,k}$ (eq. 7), and modeled river elevation, z_m, using eq. 5, as:

$$8.\quad z_m = z_b + a_s \cdot \chi_{u,k}(\,m, n, U^*, K^*) = g(a_s, m, n, U^*, K^*)$$

We estimate the robustness of our direct model, expressed through the function g, by computing the difference between modeled elevation, z_m, and measured elevation, z, using the cost function, ϕ, using the L2 norm:

$$9. \quad \phi(m, n, a_s, U^*, K^*) = ||g(a_s, m, n, U^*, K^*) - z||_2$$

Where *z* is the elevation data, typically obtained from a digital elevation model (DEM).

3.1.2 Parameterizing uplift patterns using B-spline functions

We parameterize the spatial variability of uplift, $U^*(\vec{x})$, using B-spline functions (De Boor, 1978; Piegl & Tiller, 1997). Constructed from a series of piecewise polynomial basis functions and defined between a grid of control points known as knots, B-splines serve as interpolating functions where a coefficient, *Q*, at each knot controls the shape of the uplift pattern (See Text S1). This approach provides the flexibility to modify uplift patterns by simply adjusting *Q* values without being restricted to a predetermined functional form, thus ensuring a smooth and continuous representation of spatial variability in rock uplift.

3.1.3 Parameterizing spatial Erodibility

Spatial variations in erodibility are typically driven by changes in lithology (Campforts et al., 2020; Ellis & Barnes, 2015; B. Gailleton et al., 2021; Harel et al., 2016) and the occurrence of major faults, which inherently display areal discontinuities. Thus, using continuous mathematical functions, such as B-splines, polynomials, or Gaussians, to represent variations in erodibility would misrepresent the inherently piece-wise nature of this field. We instead delineate lithological units (e.g., from geological maps) and invert for their piece-wise uniform erodibility k_i across various lithological domains (numbered by *i*)

3.1.4 Parameterizing climatic modulation of erosion

We incorporate climatic variations by weighting the drainage area with precipitation rates and computing an effective volumetric discharge, $A_Q(x)$. This method is commonly employed in fluvial topographic analysis to assess the impacts of variable precipitations, both spatially and temporally (Babault et al., 2018; Leonard et al., 2023; Leonard & Whipple, 2021). The adjusted discharge, $A_Q(x)$, at point x is defined by integrating the drainage area, A, weighted by the precipitation rate, P, from the river source, x_s, downstream to the base:

$$10.\ A_Q(x) = \int_{x_b}^{x_s} P(x)A(x)dx$$

3.2 Inversion scheme

To identify plausible combinations of a_s, m, n, U^* and K^*, we minimize the misfit between the modeled and measured elevation (eq. 9) using a Bayesian quasi-Newton scheme (Tarantola, 2005) in an iterative fashion:

$$11.\ t_{l+1} = \mathrm{t_l} + \mu(G^t C_D^{-1} G + C_M^{-1})^{-1}(G^t C_D^{-1}(z_m - z_{obs}) + C_M^{-1}(t_l - t_0))$$

Where t_l is a vector comprising all model parameters at iteration l. G is the Jacobian matrix determined using centered finite difference such that:

$$12.\ G_i = \frac{\partial \phi}{\partial m}$$

z_{obs} is a vector of observations consisting of measured elevation z, z_m is the modeled elevation of rivers computed using $g(t_l)$, C_M is the a priori covariance matrix, C_D is the observation covariance matrix, i is an index delineating model parameter and μ is a constant between 0 and 1. We employ an initial guess, t_o, assuming *m*=0.5, *n*=1, $a_s = 0.1$ as well as B-spline and erodibility coefficients that describe uniform uplift and erodibility patterns.

We configure the covariance matrix C_m with diagonal terms equal to 0.01 (standard deviation of 0.1) for the entries corresponding to m, n, and a_s, and 1 for B-spline weights and dimensionless erodibility coefficients, reflecting a lack of a priori knowledge about spatial variability in the uplift and erodibility patterns. We consider a solution m_l satisfactory when $\frac{\phi(m_{l+1})-\phi(m_l)}{\phi(m_o)} < 0.01$.

Upon reaching an optimal solution, we can use the recovered B-spline parameters to characterize the uplift pattern along the rivers used in the inversion as well as across the entire rectangular domain bounded by the river network (Text S1).The geometry of the river network may leave some knots poorly constrained due to the absence of nearby rivers. To address this, we compute uplift only within catchments feeding the rivers used in our analysis, ensuring that the involved knots have non-negligible values based on the sensitivity parameter, $diag(G^T \cdot G)$.

4 Application to synthetic landscapes

We assess the reliability of our methodology, which inherently assumes steady-state incision of channels, across a range of synthetic landscapes. These artificial terrains exhibit varying degrees of deviation from the stream power law and include hillslope diffusion, sediment deposition, orographic effects, spatial changes in erodibility, and temporal shifts in uplift rates (e.g., Leonard & Whipple, 2021; Merritt et al., 2003; Roering et al., 1999, 2001; Whipple, 2009).

4.1 Generating synthetic landscapes

We model synthetic terrains, incorporating both fluvial and hillslope erosion along with deposition dynamics based on the CIDRE model framework defined by (Carretier et al., 2016) :

$$13. \frac{dz}{dt} = \dot{d_f} - \dot{e_f} + \dot{d_h} - \dot{e_h} + U(x,y)$$

where $\dot{d_f}$ is the fluvial deposition rate, $\dot{e_f}$ the fluvial incision rate, $\dot{d_h}$ the hillslope diffusion flux, $\dot{e_h}$ the hillslope erosion rates and $U(\vec{x})$ is the imposed tectonic uplift. The fluvial component relies on a formulation originally developed by Davy & Lague (2009) where erosion and sediment entrainment are functions of stream power and sediment length deposition. The hillslope laws are a hybrid between linear and non-linear landscape diffusion models, reproducing both end-members (see Carretier et al., 2016 for full details).

We use an explicit finite difference numerical scheme to solve equation (13) where spatial discretization is done along a 100 X 100 km regular 2D grid with 400 m spacing in the *x* and *y* directions. We use different graph theory algorithms to organize our nodes into an upstream to downstream topological order (see Gailleton et al., 2024 for details on the numerical structure) and use the carving algorithm of (ordonnier et al., (2019) to resolve local minima. We employ a time step of 500 years and run synthetic models over 5 million years to ensure the landscape reaches a topographic steady state, resulting in negligible elevation variations over time. Lastly, we use $n = 1, m = 0.45$ and rock erodibility, *k*, of $2 \cdot 10^{-5}\ m\text{^}(0.9) \cdot yr^{-1}$. We parameterize the imposed tectonic uplift field using an asymmetrical 2D Gaussian- function:

$$14.\ U(x,y) = u_0 \cdot exp\ [-a(x-x_0) + 2b(x-x_o)(y-y_0) + c(y-y_0)^2]$$

Where $a = \frac{cos^{2(\theta)}}{2\sigma_x^2} + \frac{sin^{2(\theta)}}{2\sigma_y^2}, b = -\frac{sin(2\theta)}{4\sigma_x^2} + \frac{sin(2\theta)}{4\sigma_y^2}, c = \frac{sin^{2(\theta)}}{2\sigma_x^2} + \frac{cos^{2(\theta)}}{2\sigma_y^2}$, θ is the azimuth of the long-axis of the Gaussian, x_o, σ_x and y_0, σ_y are the center and width of the gaussian along the *x* and *y* directions, respectively. Lastly, we assume a characteristic uplift rate, u_0, of $1.2\ mm \cdot yr^{-1}$ (Fig. 1).

4.2 Inversion of synthetic landscapes

We apply our inversion scheme on simulated synthetic landscapes and select the 8000 most downstream nodes from the largest catchments to guarantee our inversion outputs are not secondarily influenced by the number of observations (z_{obs}). To mimic the uncertainty in real elevation data we add noise using randomly sampled values from a normal distribution centered around 0 with standard deviation, ε, of 10 m. We then invert the resulting landscapes using two different schemes. The first solves for 84 parameters including m, n, a_s and the control points for spatially-varying uplift with a 2D cubic B-spline function along 6 knots in the *y* and *x* direction. The second assumes a uniform uplift pattern and fits landscape constants m, n and a_s only (eq. 6). We estimate how well the inversions perform by comparing recovered uplift and elevation with synthetic modeled elevation and imposed uplift using the root mean square (RMS) metric:

$$15.\ RMS = \sqrt{\frac{1}{N}\sum_{i=0}^{N}(q_i^r - q_i^m)^2}$$

Where q_i^r is recovered value *i*, q_i^m imposed value *i* and *N* total number of measurements in the dataset.

4.3 Results

4.3.1 Detachment-limited scenario

We produce a synthetic landscape subject to an ellipsoidal uplift function (Table S1; Fig. S1) where erosion is exclusively detachment-limited (Fig. 1A). Once in steady state, we measure the landscape's drainage area, flow direction, and the distance between river nodes required for computing χ. We then use these landscape properties and apply two inversion mechanism: (1) solving for uplift pattern, and (2) assuming uniform uplift.

Our first inversion performs well, retrieving outputs that are almost identical to those imposed. The RMS value for uplift is 0.01, indicating that the inverted uplift for the 8,000 river nodes used closely matches the imposed tectonic uplift (Fig. 1). Additionally, our inverted elevation closely mirrors the measured elevation, with discrepancies reflecting the introduced noise, ε, leading to an RMS value of 10 meters. This accuracy is illustrated nicely by the linear shape of the final river elevation profiles in χ-space, a_s , where the scatter reflects the noise (Fig. 1C). In contrast, the inversion assuming uniform uplift returns RMS values that are 7 times higher and fails to accurately determine landscape constant m, n and a_s (Fig. 1C).

Once we have established that our inversion can accurately recover landscape properties in this idealized case, we proceed to test its limitations by challenging the assumptions it relies on.

4.3.2 Scenarios deviating from the Detachment-limited endmember

4.3.2.1 Sediment transport length

We apply our inversion scheme to synthetic landscapes featuring varying degrees of sediment deposition, hillslope diffusion, orographic effects, spatial variations in erodibility, and temporal changes in uplift rates. For the sediment deposition case, we generated 20 identical landscapes, differing only in the value of the characteristic sediment transport length (e.g., Carretier et al., 2016; Merritt et al., 2003). For transport lengths longer than $1\ km$, our inversion accurately recovers landscape parameters with RMS elevation and uplift values comparable to the noise we added, ε (Fig 2A1 & 2B1). Landscapes characterized by transport length shorter than $1\ km$ generate greater relief owing to the additional sediment deposition. Consequently, inverting these models yields less accurate inversion results, with RMS values 5 to 30 times higher for both elevation and uplift (Fig 2A1 & 2B1). Interestingly, even as the landscape deviates significantly from the detachment-limited case, the inversion aims to maintain the imposed $\frac{m}{n}$ ratio, capturing this "detachment-limited property" of the landscape (Fig. S2).

4.3.2.2 Diffusion

To test the effect of hillslope diffusion on our inversion, we modeled and inverted 50 landscapes, each employing a distinct diffusion parameters k_d controlling topographic dispersion across the landscapes (Carretier et al., 2016). For k_d smaller than $10^{-2}\ m \cdot yr^{-1}$ the inversion outputs almost perfectly retrieved the parameters of the landscape (Fig 2A2 & 2B2). For higher diffusion values of $10^{-2} - 10^{-1} m \cdot yr^{-1}$, the retrieved uplift function exhibits pronounced uncertainties but can still capture the original signal (Fig. S3). For $k_d > 10^{-2}\ m \cdot yr^{-1}$, the river network ceases to represent a typical mountain range drainage system (Fig. 2B2). This is reflected in the poor performance of the inversion showing RMS values 10-30 times higher than the best retrieval values, partly due to the lack of river nodes in the center of domain(Fig. 2A2).

4.3.2.3 Precipitation

Spatial variability in climatic conditions can also significantly influence landscapes (e.g., Molnar & England, 1990), particularly in mountain ranges with orographic precipitation on the windward flanks and drier conditions on the leeward sides (e.g., Bookhagen & Burbank, 2010). To incorporate this effect into the evaluation of our synthetic models , we index precipitation on elevation using the equation $p(z) = \alpha_o e^{-\frac{z}{h_0}}$, where α_o is precipitation at sea level, z elevation, and h_0 a reference elevation (Hergarten & Robl, 2022). To reflect reduced rainfall along the lee side of the landscape we reduce the α_o value there, effectively generating uneven precipitation $p(x, z)$ (e.g., Figs. 2B3, S3D1 and S3D2). We then simulate 50 landscapes using the effective volumetric discharge A_Q (eq. 10), modulated by precipitation $p(x, z)$ with each terrain characterized by a distinct h_0.

Our inversion assuming that water discharge simply scales with only drainage area (*A*) accurately recovers landscape parameters for $h_0 < 0.5\, km$. For h_0 values above 0.5 km, retrieval inaccuracies increase, worsening with larger values (Figs 2A3 & 2B3). However, when we use A_Q (eq. 10) in our inversion, it accurately retrieves the correct landscape parameters, effectively determining elevation, uplift (Fig 2A3), and *m*, *n* and a_s (Fig. S3). Our inversion's ability to accurately retrieve landscape parameters is particularly noteworthy given that A_Q undergoes significant changes as the landscape evolves with time and we use the values from the final timestep.

4.3.2.4 Lithology

Lithology is an additional spatially variable parameter influencing landscape evolution. We explore its significance by modeling 50 landscapes each featuring a 20 km wide zone with low erodibility, k_s, varying by up to an order of magnitude from the background erodibility, k_w, $2 \cdot 10^{-5} m\hat{}(0.9) \cdot yr^{-1}$. The sharp change in erodibility results in landscapes with two distinct topographic highs: one aligned with the imposed uplift pattern and another associated with the low erodibility zone where the ratio of altitudes between these peaks is linked to $\frac{k_w}{k_s}$ (e.g., Fig. 2B4, S5D1 and S5D2).

For $\frac{k_w}{k_s} > 0.5$ our standard inversion performs well, almost unaffected by the addition of a stronger rock section (Fig. 2A4). However, for $\frac{k_w}{k_s} < 0.5$, the standard inversion scheme struggles to accurately capture the current properties of the landscape, and the retrieved uplift values reflect the region of lower erodible domain rather than the imposed uplift shape (Fig. 2A4). However, when we invert for erodibility (see section 3.1.3) as well as U^*, m, n and a_s the inversion scheme excels in accounting for elevation and uplift pattern (Figs. 2A4 and S5). The recovered and imposed erodibility ratio are in remarkably good agreement (Fig 2A4) suggesting that our inversion scheme is capable of accounting for spatial changes in rock erodibility.

4.3.2.5 Rock uplift rate

To investigate the impact of time-varying tectonic forcing, we bring a detachment-limited landscape to a steady state and then instantaneously increase the uplift rate by a factor of three, similar to observed changes in uplift history along normal fault systems (e.g., Goren et al., 2014; Smith et al., 2024). We proceed to simulate the landscape for an additional 1.6 million years until it reaches a new equilibrium (calculated using Equation (3) ;Fig. S6) and invert landscapes snapshots retained at intervals of 0.1 million years.,

Our inversion responds to the step change in uplift rate with a minor increase in RMS values for the retrieved elevation. Conversely, the inversion shows greater deviations in the recovered uplift pattern and in the m, n and a_s values than in elevation (Figs. 2A5, 2B5 & S7). This is because the inversion effectively compensates with adjustments in other parameters to return accurate elevation values. This illustrates the challenge of determining whether a natural landscape is in steady state based solely on elevation errors. After about half the time needed to reach equilibrium, the inversion returns values that align well with the imposed parameters (Fig. 2A5). This stabilization in parameter retrieval is clearly illustrated by a_s values (incorporating the updated u_0 value) which reach their new steady-state levels approximately 0.8 million years after the step change. We attribute the inversion's ability to retrieve the imposed values before the entire landscape reaches steady state to the fact that a significant portion of the landscape is already in equilibrium, with only the upstream sections of rivers still in transition. This is evidenced by the large misfit values at the river tips, which, unlike in steady-state conditions, are more evenly distributed across the landscape (Fig. S8). We note that we observe a similar pattern in landscapes subjected to temporal changes in uplift pattern over a given time period (Text S2 & Fig. S8).

5 Application to natural landscapes

5.1 Selection of sites

To test the real-world applicability of our inversion scheme, we apply it to both divergent and convergent tectonic settings. For the divergent setting, we analyze five landscapes shaped by normal faults, where our understanding of the crust's flexural response to faulting provides a reliable test bed for comparing our inverted uplift patterns. For the convergent setting, we focus on a well-studied, approximately 200 km-wide section of the Himalayas and compare our results to previous uplift estimates derived from geomorphological markers.

5.1.1 Landscapes shaped by normal faults

We apply our inversion methodology to natural landscapes shaped by half-graben border faults where kilometer-scale offset along the fault flexes the brittle upper crust, yielding a 1-D rock uplift field that decreases with across-strike distance from the fault (Fig S10; Weissel & Karner, 1989). Thicker and stronger faulted layers typically produce longer uplift decay lengths, extending further into the footwall. This relatively simple pattern makes it an appealing benchmark case, and has been leveraged in previous geomorphological tectonic studies (e.g., Goren et al., 2014; Ellis & Barnes 2015). Recovering systematic trends in the uplift shape consistent with flexural properties of several landscape would provide additional constraints on the validity of our inversion.

To this end, we study five landscapes with varying faulted layer thicknesses (Table S2; Olive et al., 2022): The Paeroa Range (Paeroa fault ,New Zealand), Sandia Mountains (New Mexico, USA), Wassuk Range (Nevada, USA), Lehmi Range (Lehmi Fault, Idaho, USA), and Kipengere Range (Livingstone Fault, Lake Malawi, Tanzania). We analyze river sections located far from fault tips

(Densmore 2007;Ellis & Barnes, 2015), ensuring that uplift is predominantly a function of distance from the fault, allowing us to use the faster 1D inversion. However, to demonstrate the applicability of our 2-D inversion scheme, we apply it to the Lemhi range where we specifically focus on the southern section near the fault tip because its uplift pattern is well-documented and has been shown to diminish southward (Fig. S10;Densmore et al., 2007).

We include erodibility variations for the Sandia mountains, as they feature two clear and distinct lithological domains comprising predominantly limestone on the Eastern side and granite on the Western side (Williams & Cole, 2007), which typically show different erosional properties (Fig 3C2). We assume uniform erodibility in other studied landscapes as these exhibits relatively uniform lithology. Lastly, we note that we did not account for spatial changes in precipitation here. The Kipengere Range showed little evidence of a correlation between precipitation and altitude in documented rainfall trends in the past 23 years (Fig S11; Global Precipitation Measurement; GPM; Huffman et al., 2015) despite its 1.5 km relief and an expected strong orographic effect. This suggests that orographic effects are even less important in the other gentler landscapes.

5.1.2 The Himalayas

We apply our inversion scheme to a well-studied, approximately 200 km-wide section of the Himalayas, where previous studies have identified high uplift rates occurring around 100 km from the main Himalayan thrust, with slower uplift rates observed farther away (Dal Zilio et al., 2021; Godard et al., 2014; Lavé & Avouac, 2001)). We exclude the Siwalik Hills from our analysis as rivers in this region are not predominantly detachment-limited. Additionally, we omit catchments north of the Himalayan water divide extending to the Tibetan Plateau, as these require separate, higher base levels, which would limit the spatial extent of our analysis.

Our inversion accounts for four distinct erodibility sections, delineated by the main lithological units in the area (Fig 4C;Carosi et al., 2018). To incorporate the pronounced climatic patterns in the Himalayas (e.g., Bookhagen & Burbank, 2010), we compute A_Q using eq (10), based on the average spatial distribution of the past 23 years of satellite-based precipitation data (Fig. 4D; Huffman et al., 2015).

5.2 Inversion of natural landscapes

We use 30 m-DEM of landscapes obtained by the Shuttle Radar Topography Mission (Farr et al., 2007) . We extract nodes (pixels) corresponding to major rivers (Figs. 3B1-3B5 and 4A), defined as those draining areas larger than a set threshold and above a set base level elevation (Table S2). These thresholds are carefully selected to balance computational efficiency for the inversion calculations with an accurate representation of the landscape's fluvial sections. For landscapes shaped by normal faults, our aim is to include river nodes that cover the entire decay length of the fault-induced uplift. However, this is often complicated by river nodes near the fault, which are typically located on hanging wall-facing cliffs that drain small areas or lie underwater. Consequently, we calculate the rivers' distance from the outlet, drainage area, and elevation (O'Callaghan & Mark, 1984), and rotate their geographical coordinates to align with an along-fault strike and across-fault strike coordinate system. We estimate their connectivity and flow path using the steepest descent algorithm (O'Callaghan & Mark, 1984).

We compute multiple inversion scenarios for each landscape, varying the number of B-spline nodes, ensuring the distance between B-spline nodes is at least 5km (Text S1). We report the inversion that minimizes the Akaike Information Criterion (AIC) (Akaike, 1974; Bishop, 2006). The AIC includes a penalty term to prevent potential overfitting caused by the addition of superfluous parameters to the model (Text S3). We also assume an elevation uncertainty of 30 meters, a value that has been deliberately increased from the reported SRTM dataset uncertainty. This additive inflation addresses our model's limitations in capturing detailed terrain features, as highlighted in the synthetic inversion cases. Employing such an approach is common practice across various parameterizations in physical modeling, aiming to better represent the inherent uncertainties without exhausting every detail (e.g., Anderson, 2007). Lastly, we note that for the Malawi landscape case, we set the covariance matrix to values of 10^{-4} (standard deviation of 10^{-2}) for *m* and *n*. This adjustment was necessary to avoid inverted *m* and *n* values that produced unrealistically long knickpoint travel times (eq. 3).

5.3 Results

5.3.1 Landscapes shaped by normal faults

Our 1D inversions consistently reveal an uplift pattern that decreases with greater distances from the fault along the footwall (Fig. 3A-D). The recorded wavelength correlates with the thickness of the brittle faulted layer constrained by the maximum depth of recorded earthquakes (Olive et al., 2022; Table S2; Figs. 3A1-A4) where the Paeroa Range (Fig. 3A1) exhibits the narrowest uplift wavelength followed by the Sandia (Fig. 3A2), Wassuk (Fig. 3A3), and Kipengere (Fig. 3A4) ranges.

For the Sandia Mountains, inversions assuming both uniform and variable erodibility yield nearly identical uplift wavelengths. However, the first yields an unrealistic peak in the uplift field at a distance of 8 km from the fault which we attribute to variations in erodibility (Fig. 3A2). An inversion that accounts for a different erodibility in the Western and Eastern sides of the range indeed yields a more straightforward uplift field that continuously decays with distance to the fault. It also produces less scatter in χ values (Fig. 3B2) and determines that Sandia granite (West side) is 2.2 times more erodible than the Madera formation limestone (East side, Fig. 3C2). The latter is consistent with the notion that high infiltration rates over carbonate landscapes deprive rivers from water and therefore erosive power, while much greater surface runoff enhances granite denudation. This results underscores the importance of considering variable erodibility when inferring tectonic uplift fields.

We highlight that our inversion method is designed to recover the coefficients controlling the B-spline knots (see Figs. S12-S15 for the posterior distributions of all inverted parameters) , which can be used to describe uplift not only along the rivers utilized in the inversion but also across all catchments feeding those rivers (see section 3.5.1). While this capability is clearly demonstrated in the 1D inversion cases (Figs. 3C1-4), its true strength lies in capturing complex spatial attributes across two dimensions. For example, our 2-D inversion for the Lemhi landscape effectively captures the spatial variations in uplift expected near the tip of a normal fault within the Lemhi Range. It shows diminishing uplift within 10 km to the fault tip (Fig. 3A5), aligning with previously documented k_{sn} values in the region (Densmore et al., 2007), and a general decrease in uplift with increasing distance from the fault axis (Fig. 3C5). These observations demonstrate our model's ability to accurately infer two-dimensional variations in uplift.

Similar to our synthetic landscapes (Figs. 1C, S2-5), inverting for uplift patterns yields RMS values that are 2-3 times better than those assuming a uniform uplift pattern (Fig. 9). This is visually supported by the tight alignment of χ values around the recovered a_S particularly in the Wassuk range case where χ values that do not account for uplift gradients form three distinct branches in contrast to the neatly aligned χ values for the inversion that accounts for uplift variations (Fig. 3B3). Additionally, the average recovered m/n ratio is closer to θ = 0.45, a value considered typical for natural landscapes (Boris Gailleton et al., 2021; Mudd et al., 2014; Snyder et al., 2000). The Wassuk Range shows relatively large deviation with an m/n ratio of 0.22. However, when we invert the landscape while fixing n=1 and m=0.45 we recover an uplift pattern that closely resembles the original with an RMS value larger by 1.4 (Fig. S16).

We note that the Malawi landscape exhibits the highest RMS value compared to other landscapes shaped by normal faults (Fig. 3). The steep, incised topography of the Kipengere Ridge indicates strong fluvial incision driven by detachment-limited processes near the fault. However, fluvial incision driven by the Livingstone fault system extend into smoother, sediment-filled valleys about 40 km away, where hillslope diffusion and sediment deposition contribute to elevation misfits. These contrasting landscape features likely explain the larger misfits in Malawi compared to other landscapes with smaller RMS values.

5.3.2 The Himalayas

Our inversion results for the Himalayan section reveal a distinct region of uplift approximately 100 km N-NE of the main frontal thrust, extending from the eastern to the western end of the study area (Fig. 4A). This finding aligns well with previous estimates (Fig. 4G) derived from fluvial incision rates observed in terraces, channel geometry (Lavé & Avouac, 2001), ^{10}Be

concentrations in detrital sediments (Godard et al., 2014), and 1-D river profile analysis (Meade, 2010). Additionally, we identify a second uplift peak closer to the frontal thrust on the southwestern end. The uncertainty associated with this peak is larger (Fig. 4C) due to the sparse river network in the region, which limits the constraints on the B-spline coefficients and reduces our confidence in interpreting this feature.

In contrast to the Sandia Mountains (Fig. 3A2), where erodibility values exhibited significant contrast and strongly influenced the inverted uplift patterns, the recovered erodibility values in the Himalayas (e.g., Fig. 4D) are relatively uniform, with values within one standard deviation of each other (Table S3). This suggests that spatial variations in erodibility does not play a major role in shaping the landscape in this section of the Himalayas.

To assess the influence of climate patterns, we performed an additional inversion that excluded the effects of variable precipitation. Although this inversion resulted in RMS values that were higher by a factor of 1.3 (Fig. 4B), it still revealed similar overall features, including an uplift peak extending from east to west (Fig. 4F). Interestingly, when precipitation variability was excluded, the highest uplift region shifted from the western side to the central area of the domain. This shift illustrates how increased rock uplift is required to offset larger drainage areas in the west when accounting for variable precipitation (Fig. 4A).

6 Discussion

6.1 Applicability and limits of the methods: Insights from Synthetic landscapes

By examining synthetic landscapes we show that pronounced hillslope diffusion and sediment transport lead to reduced accuracy of recovered landscape properties. Significant sedimentation in mountain ranges depart from the detachment-limited models we use, leading to discrepancy between inverted and imposed uplift (Fig. 2B1). Satellite imagery offers a reliable method to identify regions with pronounced sediment cover, allowing us to focus on basins with predominantly bedrock rivers (e.g., Perron & Royden, 2013; Wobus et al., 2006).

The impact of hillslope diffusion is more uniform across the landscape and thus more challenging to circumvent. However, our synthetic landscape analyses suggest that only in case of exceptionally pronounced hillslope diffusion do our recovered uplift patterns starkly diverge from the imposed uplift (see Litwin et al., in rev. for a corrective solution). Such high values of hillslope diffusion should form natural landscapes with smooth features that are easy to identify and avoid (e.g, Fig. 2B2). We note that our synthetic hillslope diffusion model does not account for changes in diffusion rates across landscapes (e.g., Auzet & Ambroise, 1996; Bontemps et al., 2020; Matsuoka, 1998). Additionally, our underlying assumption is that channel width is a power-law function of discharge manifested as a change in the effective exponent m. In reality, however, river channels width may vary locally, with narrower channels increasing erosion (Lavé & Avouac, 2001; Yanites et al., 2010) ,which in our case would likely result in unrealistic high inverted uplift pattern.

Our study of synthetic landscapes adjusting to a change in uplift rates and patterns reveals that if more than half the required time to reach a new equilibrium has passed, our inversion accurately recovers the uplift signal (Fig. 2A5). In our simulations, temporal changes are modeled as instantaneous steps while in natural settings, these variations may unfold over extended periods. For example, Smith et al. (2024) used river profiles along the normal fault-bound Wasatch Range, demonstrating that uplift rates fluctuate temporally up to threefold within as little as 400 ky suggesting that the landscape may never achieve quasi steady state. Similarly, when we model changes in uplift rates over comparable durations, our inversion method successfully recovers uplift patterns closely resembling the imposed ones (Text S3; Fig S17), despite the landscapes being far from steady state. This echoes our findings from instantaneous step changes experiment (Fig. 2A5), confirming that even when landscapes are not in steady state, our inversion can retrieve uplift patterns that mirror the imposed ones. This indicates that when we apply our inversion to natural landscapes, we likely extract a value of a_s that reflects a time-averaged window and an uplift pattern that shows minor deviation from the time-averaged tectonic uplift. This is partly because working in the χ framework lets us treat the river network as a cohesive system, integrating the contributions of all river nodes, as opposed to local approaches such as k_{sn}.

In contrast, temporal variations in spatial uplift pattern are typically slower and less frequent. Adjustments in fault orientation or dip angle, which can alter uplift patterns, are either slow and progressive (e.g.,Olive & Behn, 2014; Oryan & Buck, 2020) or result in the formation of new faults rather than modifying existing ones (e.g., Taylor & Switzer, 2001). These new faults are likely to form far from the original faults and may not significantly impact the associated uplift pattern. Our synthetic landscape experiments exploring the effects of gradual temporal changes in uplift patterns demonstrate that, as long as the imposed changes are slow enough, our method accurately extracts uplift patterns that closely resemble the original ones (Text S4; Fig S18).

Our synthetic landscape analyses also demonstrate that spatial variations in erodibility and precipitation can significantly alter the recovered uplift pattern with discrepancy amounting to RMS values of 10-5 times the original signal (Fig. 2A4). Nevertheless, we demonstrated that the inversion is capable of accounting for those. This is crucial as current methods to extract uplift patterns from landscapes often rely on k_{sn} (e.g., Castillo et al., 2014; Densmore et al., 2007; Ponza et al., 2010; Su et al., 2017) which cannot directly distinguish between erodibility and uplift given spatial varying erodibility. Our method offers a way to discern the two provided that we can predefine regions with different erodibility levels based on lithological maps.

6.2 Performance on natural landscapes

Our analysis of natural landscapes highlights the effectiveness of our inversion method. For landscapes shaped by normal faults, we demonstrate that the decay length of the uplift field away from the fault is directly linked to the thickness of the brittle upper crust (Figs. 3A1-4), consistent with standard models of normal fault-induced flexure, where a thicker elastic layer typically produces a broader uplift profile (e.g., Goren et al., 2014; Nadai, 1963; Weissel & Karner, 1989) We demonstrate that our method can robustly extract this signal, even when it is intricately linked with spatial variations in erodibility (Figs. 3A2). Additionally, we retrieve smaller uplift rates around the Lemhi fault tip (Fig. 3A5), aligning with previous uplift estimates (Densmore et al., 2007) and the notion that slip vanishes over a short distance near fault tips (Ellis & Barnes, 2015; Roberts & Michetti, 2004). Our analysis of the Himalayan landscape (Fig. 4) further validates the effectiveness of our method in retrieving realistic uplift patterns while accounting for climatic variations, showing strong alignment with previous estimates based on geomorphological markers (Fig 4G). This consistency across different tectonic settings underscores the robustness of our inversion approach in accurately recovering uplift patterns from natural landscapes.

This said, pinpointing which aspects of the retrieved signal are linked to temporal changes presents an intriguing challenge. Our analysis of synthetic landscape shows we can recover uplift pattern similar to the imposed one, even when introducing a fivefold fluctuation in the uplift rate through time (Text S3;Figs. S17). The uplift field driven by tectonics should only change steadily (e.g., as the fault rotates to different dips, or lengthens along strike), as we expect major disruptions in uplift to be due to the initiation of new faults / abandonment of old ones (see section 5.1).

This leads us to focus on determining whether the signal associated with slip on a currently active fault ongoing fault slip has reached equilibrium. The time required for a knickpoint to travel upstream from the base level, calculated using eq. (3) and our recovered parameters a_s, m, n, along with estimates of uplift rate u_0 and erodibility value k_0, suggests that all but one of the normal fault-bound landscapes have reached equilibrium since fault initiation (see Text S5; Fig S19; Table S2). The Malawi landscape exhibits a travel time of approximately 35 million years, extending well beyond the initiation time of the Livingstone Fault, estimated at ~23 million years (Mortimer et al., 2016). Even if we consider the time to reach steady state is cut by half as indicated by our analysis of synthetic landscapes, it is likely that regions far from the fault have not reached a steady state. This could explain the transition to a more gradual incline in the recovered uplift pattern observed approximately 10 km from the fault (Fig. 3D).

In the Himalayas, we are fortunate to have an abundance of geomorphological markers that measure uplift and denudation rates across various timescales, allowing us to qualitatively assess whether the landscape is in a quasi-steady state. These markers include rock-uplift rate estimates from river-profile analyses (Lavé & Avouac, 2001), ^{10}Be concentrations in fluvial sediments (Godard et al., 2014), apatite fission-track cooling ages (Robert et al., 2009) and thermochronological data (Herman et al., 2010) , capturing processes operating over time scales ranging from thousands to millions of years. All these geomorphological markers indicate a peak in uplift rate at approximately 100 km from the main frontal thrust (Fig. 4G). This consistency in spatial patterns across different temporal scales highlights the temporal persistence of tectonic signals and suggests that the Himalayan landscape may approach a steady state.

Additional support for the success of our inversion lies in its ability to extract θ values that closely aligned with the expected value of ~0.45 (Figs. 3 & 4). This suggests that our method remains effective even in the absence of strong constrains on the reference concavity index ($\frac{m}{n}$), a parameter challenging to constrain (Gailleton et al., 2021; Mudd et al., 2014, 2018; Snyder et al., 2000). Nonetheless, we note that our initial choice of *m* and *n* values may lead to convergence at a local minimum (Tarantola, 2005) which may prevent exploring minima associated with similar concavity values with different *m* and *n* values. Using alternative approaches such as the Metropolis-Hastings Markov Chain Monte Carlo (MCMC), would minimize the likelihood of converging to a local minima by thoroughly sampling the posterior probability density function and providing a comprehensive exploration of the parameter space. (e.g., Dal Zilio et al., 2020; Gardonio et al., 2018; Jolivet et al., 2020). However, MCMC is computationally expensive, requiring millions of forward model evaluations, making it impractical for the more than 2500 separate inversions conducted in this study. Inverting large-scale landscapes, on the other hand, would necessitate significantly more B-spline nodes and inverted parameters, diminishing the benefits of the quasi-Newton scheme and making MCMC a more appropriate candidate for the choice of inversion scheme.

Finally, our analysis of natural landscapes provides an opportunity to examine the theoretical predictions of lithospheric flexure (Nadai, 1963; Weissel & Karner, 1989). The deformation associated with kilometer long offset accommodated along normal faults is typically approximated as a thin, broken elastic plate of thickness, T_e, flex above a viscous half-space. This predicts that uplift due to flexure diminishes exponentially with greater distance from the fault, as $e^{-\frac{x}{\alpha_b}}$,and that uplift wavelength, α_b, is linearly proportional to $T_e^{\frac{3}{4}}$ by a coefficient that reflects the elastic properties of the lithosphere (Text S6;Nadai, 1963). Adopting typical properties of the lithosphere suggests a relationship of $\alpha_b = 45 \cdot T_e^{\frac{3}{4}}$, however, our derived uplift profiles, in conjunction with the elastic plate thickness, suggest a correlation characterized by a coefficient of 1.5, significantly lower than the expected value of 45 (Text S6; Fig. S20-21). This discrepancy has also been observed for the Basin and Range's Inyo mountains (Goren et al., 2014) and likely arises from the theory's neglection of inelastic flexure and isostatic adjustment associated with erosion and the transportation of sediment to the hanging wall basins. Advanced numerical simulations that incorporate surface processes and the dynamic behavior of the crust and lithosphere could provide further insights into these discrepancies (e.g., Olive et al., 2022).

6.3 Future applications of our method

The success of our method in recovering uplift patterns while rigorously untangling climatic, lithological and tectonic drivers in both synthetic and natural landscapes suggests that it could be applied to other tectonic settings where knowledge of long-term uplift rates is limited.

One exciting application of our method is its ability to untangle climatic and tectonic signals, shedding light on the long-standing question of the relative roles of climate and tectonic forcing in the evolution of orogenic regions such as the Andes and Himalayas (e.g., Leonard et al., 2023; Montgomery et al., 2001; Whipple, 2009; Molnar & England, 1990). Our findings indicate that the impact of climate on the section of the Himalayas we studied is relatively negligible (e.g., Godard et al., 2014) as our recovered uplift patterns remained consistent and aligned well with geomorphological indices regardless of climate variability (Fig. 4). Our method could also be applied to explore the effects of potential wetter or drier climatic periods by modifying the climate patterns applied in the inversion. For landscapes with well-established uplift patterns, we could even adapt our approach to invert for long-term climate trends using the same B-spline functions to describe climatic variations.

Another compelling application of our method is its ability to recover long-term uplift trends to help constrain seismic hazards along subduction zones, which produce the most destructive earthquakes on Earth. This is particularly relevant in light of recent evidence showing that geodetically locked areas of subduction megathrusts, which produce short-term interseismic surface uplift (e.g., Lindsey et al., 2018; Oryan et al., 2023; Steckler et al., 2016), show systematic correlations with long-term uplift patterns (Fig. 4G) shaped over thousands of years (Jolivet et al., 2020; Malatesta et al., 2021; Saillard et al., 2017). This correlation is even observed in the

Himalayan section we studied (Fig. 4G) and is attributed to the accumulation of irreversible strain during the interseismic period, generating a spatially variable, permanent uplift field recorded by the landscape over many seismic cycles (Oryan et al., 2024). Our inversion method opens the door to leveraging these time-averaged signals captured in landscapes over tens of thousands of years and hundreds of earthquake cycles, offering valuable insights into persistent plate coupling and the associated seismic hazards over extended timescales.

7 Figures

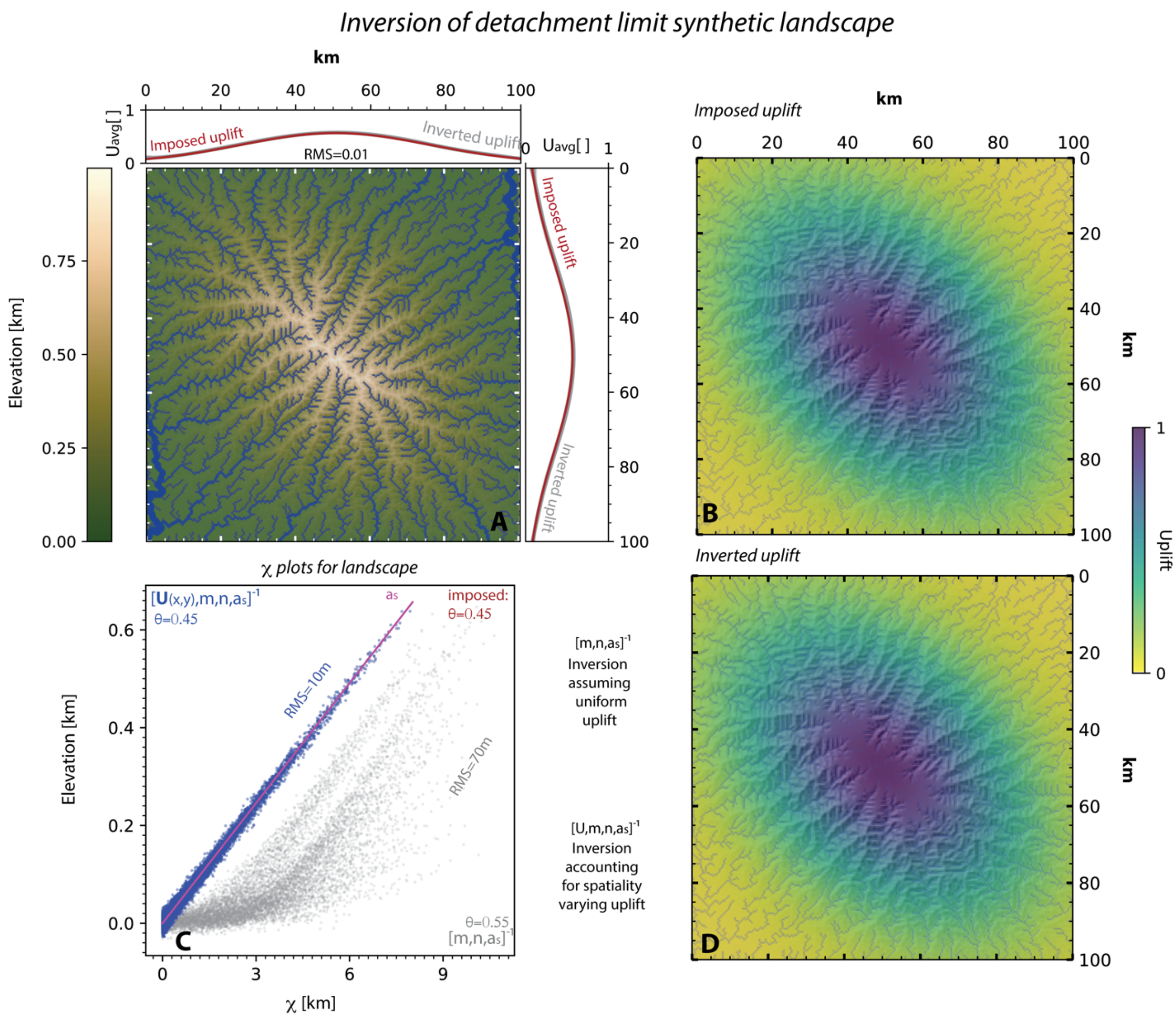

Figure 1 – Inverted detachment limited synthetic landscape. A – Landscape terrain. Blue dots show 8000 river nodes used to constrain the inversion with dot size proportional to the drainage area. Marginal plots show average uplift along axis. Imposed uplift is shown in red curve and 500 samples randomly drawn from the inverted uplift posterior distribution and extrapolated to the domain are shown in grey. B – Imposed uplift function used during the simulation of the landscape. Dots show river nodes used in the inversion. C – Points show measured elevation (z_{obs}) for 8000 river nodes and χ values derived from best inverted solution. Blue and grey denote inversion results including and excluding uplift, respectively. D – Best inverted uplift solution extrapolated for the entire domain. Dots mark river nodes used to constrain the inversion.

Inversion of synthetic landscapes deviating from detachment limited model

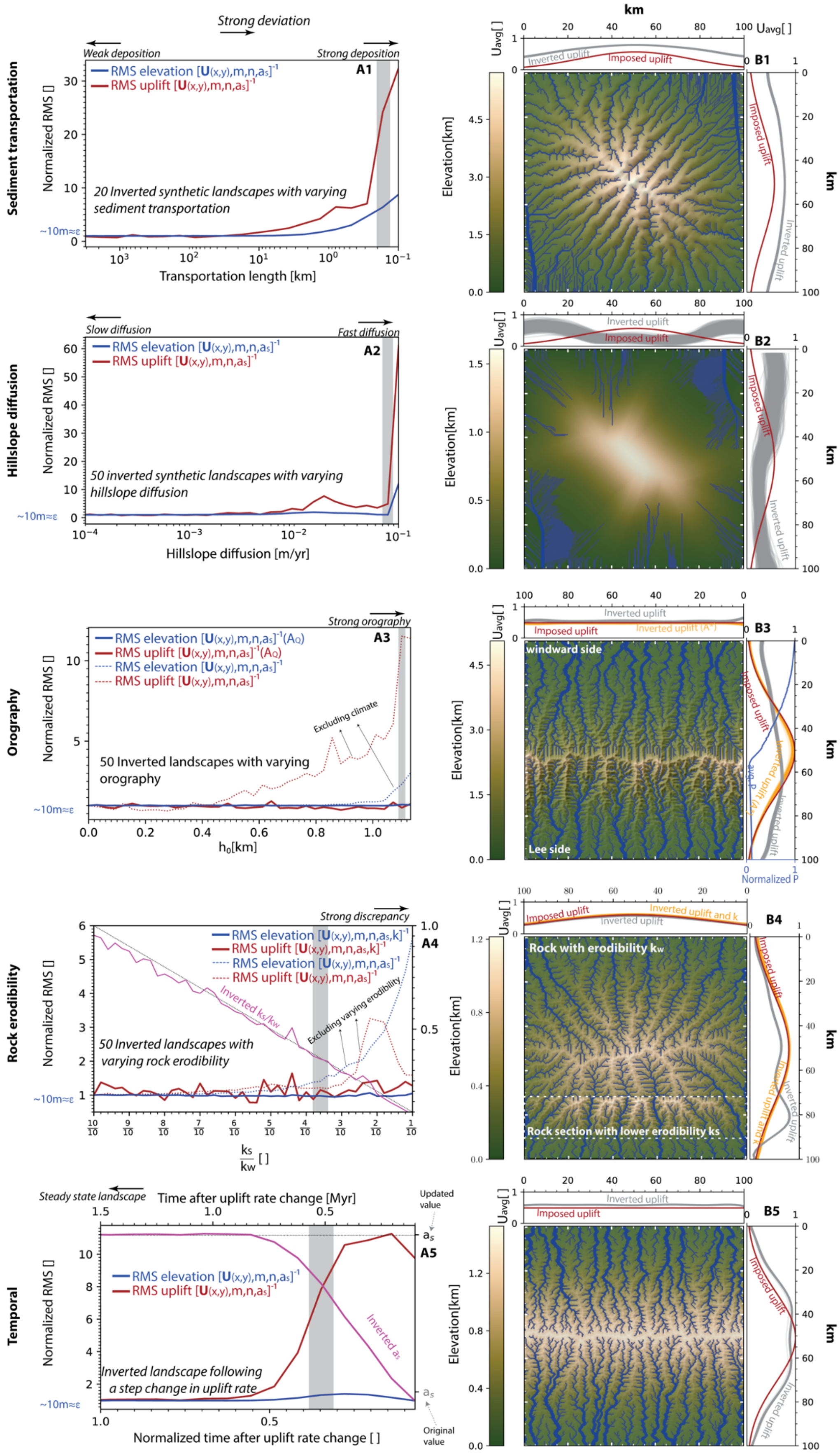

Figure 2 – Inverted synthetic landscapes deviating from the detachment limited model showing varying degrees of hillslope diffusion (1), sediment deposition(2), orographic effects(3), spatial variations in erodibility(4), and temporal changes in uplift rates(5). A - RMS values for elevation and uplift and normalized with respect to value obtained for the detachment limited landscape (Fig 1). ε denote error we introduced amounting to 10m (See section 4.2). Grey vertical line shows an example landscape described in panel B. B -Landscape Elevation. Blue dots show 8000 river nodes used for the inversion with dot size proportional to the drainage area. Marginal plots show average uplift along axis. Imposed uplift is shown in red curve and 500 samples randomly drawn from the inverted uplift posterior distribution and extrapolated to the domain are shown in grey and orange colors. Panels A4 and A5 show the inverted and imposed parameters k_w/k_s and a_s in magenta and dashed black line, respectively. The x-axis in Panel A5 displays time in million years (top) and as a fraction of the time it takes for the landscape to reach steady state(bottom).

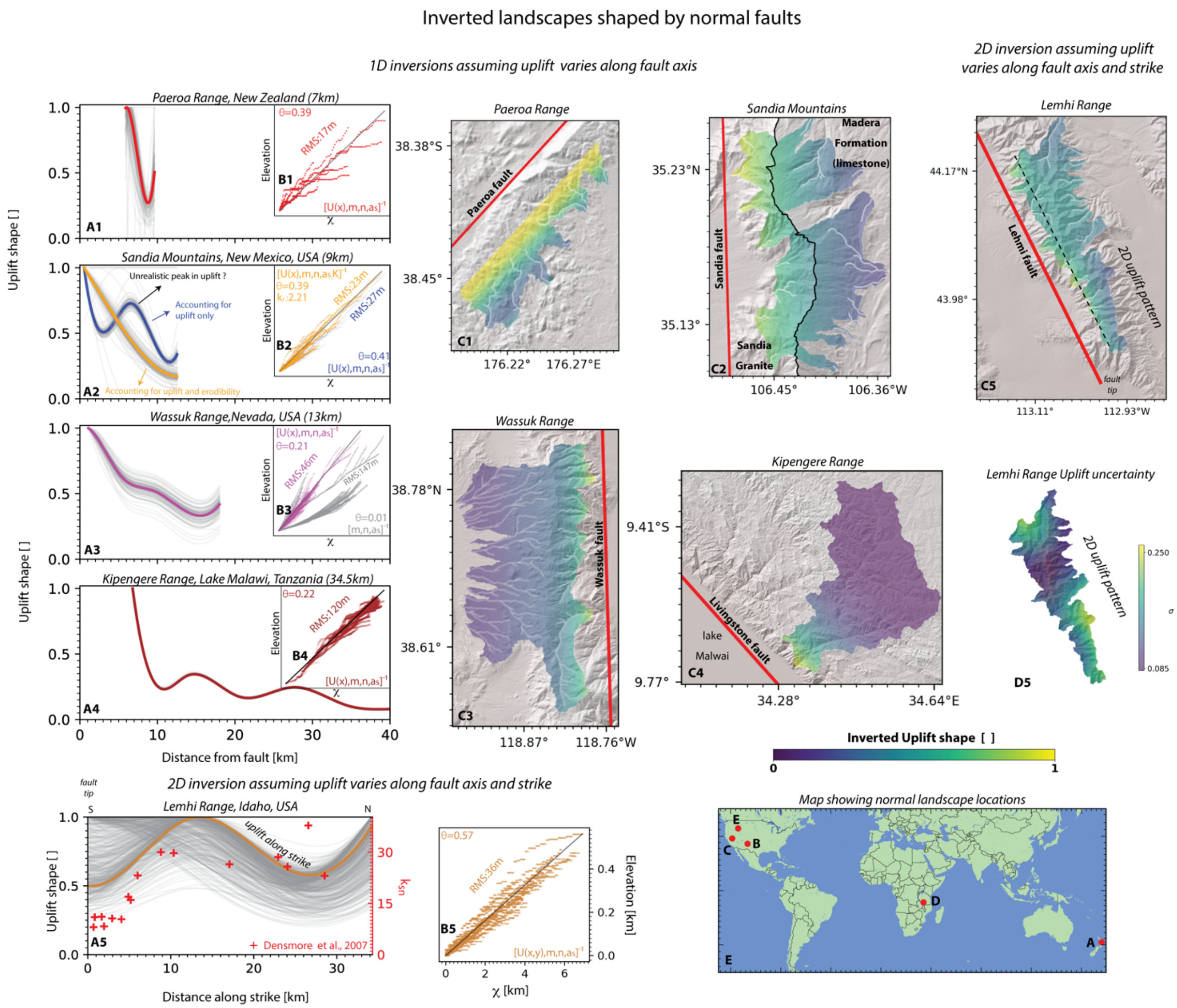

Figure 3 – 1D (1-4) and 2D (5) inversions of five natural landscapes shaped by normal faults. A – Best-fitting uplift pattern as a function of distance from the fault is represented by colored curves, with 500 uplift solutions randomly sampled from the posterior distribution shown as grey lines. In A5, the uplift is displayed along strike, following the dashed black line shown in C5. Red markers indicate k_{sn} values computed by Densmore et al. (2007). B - Colored dots represent the χ values for the best-fitting solution for river nodes used in the inversion. Black line marks the inverted slope a_s. Elevation indicates the relief from the base level. The parameter θ denotes the ratio of the inverted m/n values. In A2, k_r shows the erodibility ratio for two inverted rock sections in Sandia. C - The uplift pattern is displayed within the catchments feeding the rivers used in the inversion, highlighted in light white. The fault position is indicated by a red line. In C2, the positions of two lithological sections are shown to the right and left of the ridge line, which is marked by a black line. D – Uplift standard deviation, represented by the colormap, is calculated

by evaluating the uplift at each pixel using 500 samples randomly drawn from the posterior distribution. E – map showing landscapes locations.

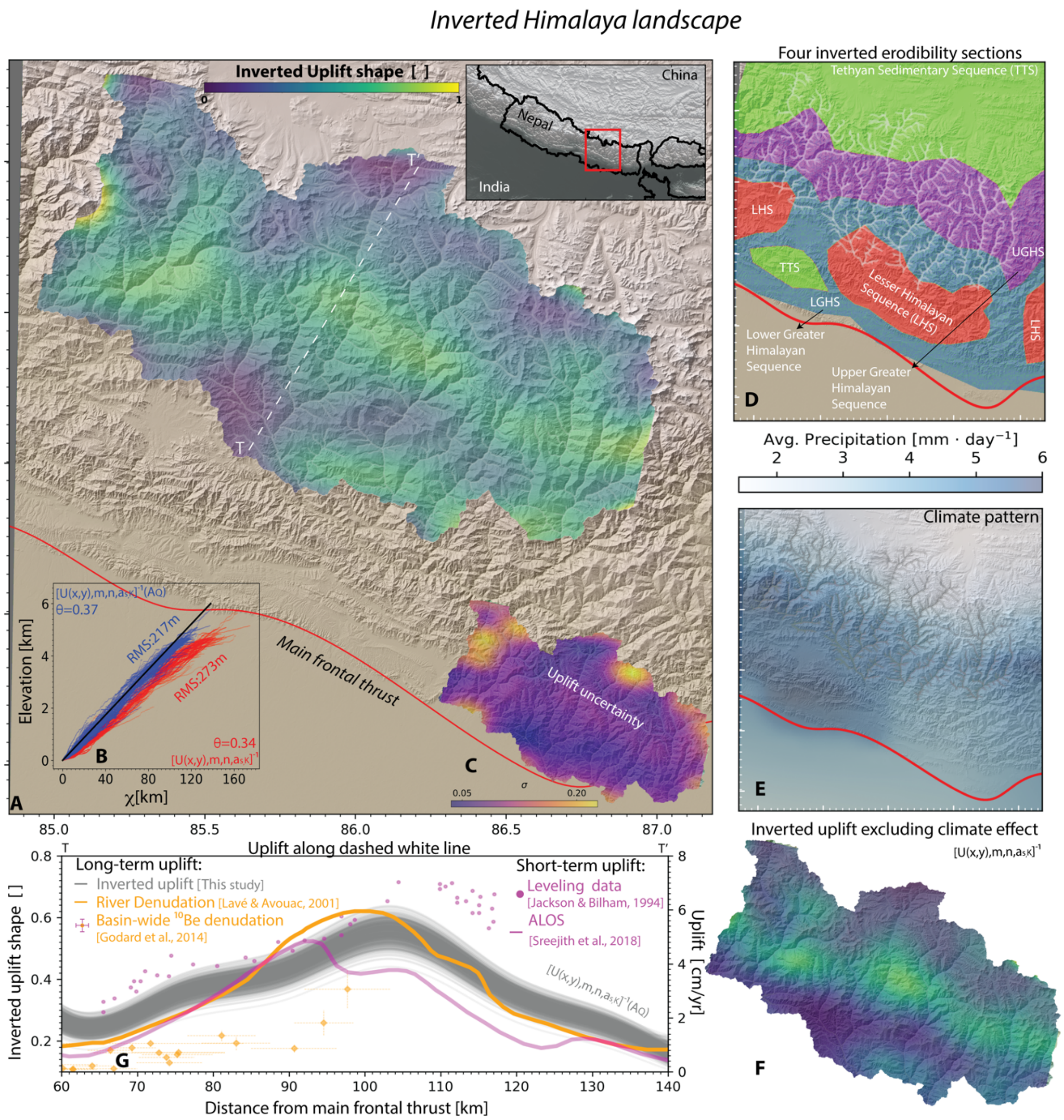

Figure 4 – Inversion results for Himalaya landscape. A – Best-fitting uplift pattern for the inversion including climate effect is displayed within the catchments feeding the rivers used in the inversion, highlighted by light white does. White dashed line shows the profile used to plot uplift in panel F. B **-** Colored dots represent the χ values for the best-fitting solution for river nodes used in the inversion including (blue) and excluding (red) climate effects. Black line marks the best fitting inverted slope a_s. Elevation indicates the relief from the base level. The parameter θ denotes the ratio of the inverted m/n values. C- Uplift standard deviation is calculated by evaluating the uplift at each pixel using 500 samples randomly drawn from the posterior distribution. D – Four distinct lithological sections (Carosi et al., 2018) used to constrain the spatial variability of four inverted erodibility values. River nodes used in the inversion are marked by white dots. E – Average climate pattern used to constrain the climate drainage area, A_Q (section 3.1.4). River nodes used in the inversion are shown by gray dots. F – best fitting uplift

pattern for the inversion excluding climate effects. G– Gray curves represent 500 uplift patterns randomly drawn from the posterior distribution along a line perpendicular to the main frontal thrust. Long-term (Godard et al., 2014; Lavé & Avouac, 2001) rates and short-term (Jackson & Bilham, 1994; Sreejith et al., 2018) uplift recorded during the interseismic period are indicated by orange and magenta colors, respectively.

8 References

Akaike, H. (1974). A new look at the statistical model identification. *IEEE Transactions on Automatic Control*, *19*(6), 716–723. https://doi.org/10.1109/TAC.1974.1100705

Anderson, J. L. (2007). An adaptive covariance inflation error correction algorithm for ensemble filters. *Tellus A: Dynamic Meteorology and Oceanography*, *59*(2), 210. https://doi.org/10.1111/j.1600-0870.2006.00216.x

Armijo, R., Meyer, B., King, G. C. P., Rigo, A., & Papanastassiou, D. (1996). Quaternary evolution of the Corinth Rift and its implications for the Late Cenozoic evolution of the Aegean. *Geophysical Journal International*, *126*(1), 11–53. https://doi.org/10.1111/j.1365-246X.1996.tb05264.x

Auzet, A.-V., & Ambroise, B. (1996). Soil Creep Dynamics, Soil Moisture and Temperature Conditions on a Forested Slope in the Granitic Vosges Mountains, France. *Earth Surface Processes and Landforms*, *21*(6), 531–542. https://doi.org/10.1002/(SICI)1096-9837(199606)21:6<531::AID-ESP606>3.0.CO;2-B

Babault, J., Viaplana-Muzas, M., Legrand, X., Van Den Driessche, J., González-Quijano, M., & Mudd, S. M. (2018). Source-to-sink constraints on tectonic and sedimentary evolution of the western Central Range and Cenderawasih Bay (Indonesia). *Journal of Asian Earth Sciences*, *156*, 265–287. https://doi.org/10.1016/j.jseaes.2018.02.004

Bishop, C. M. (2006). *Pattern recognition and machine learning* (Vol. 4). Springer. Retrieved from https://link.springer.com/book/9780387310732

Bontemps, N., Lacroix, P., Larose, E., Jara, J., & Taipe, E. (2020). Rain and small earthquakes maintain a slow-moving landslide in a persistent critical state. *Nature Communications*, *11*(1), 780. https://doi.org/10.1038/s41467-020-14445-3

Bookhagen, B., & Burbank, D. W. (2010). Toward a complete Himalayan hydrological budget: Spatiotemporal distribution of snowmelt and rainfall and their impact on river discharge. *Journal of Geophysical Research: Earth Surface*, *115*(F3). https://doi.org/10.1029/2009JF001426

Campforts, B., Vanacker, V., Herman, F., Vanmaercke, M., Schwanghart, W., Tenorio, G. E., et al. (2020). Parameterization of river incision models requires accounting for environmental heterogeneity: insights from the tropical Andes. *Earth Surface Dynamics*, *8*(2), 447–470. https://doi.org/10.5194/esurf-8-447-2020

Carosi, R., Montomoli, C., & Iaccarino, S. (2018). 20 years of geological mapping of the metamorphic core across Central and Eastern Himalayas. *Earth-Science Reviews*, *177*, 124–138. https://doi.org/10.1016/j.earscirev.2017.11.006

Carretier, S., Martinod, P., Reich, M., & Godderis, Y. (2016). Modelling sediment clasts transport during landscape evolution. *Earth Surface Dynamics*, *4*(1), 237–251. https://doi.org/10.5194/esurf-4-237-2016

Castillo, M., Muñoz-Salinas, E., & Ferrari, L. (2014). Response of a landscape to tectonics using channel steepness indices (*k*sn) and OSL: A case of study from the Jalisco Block, Western Mexico. *Geomorphology*, *221*, 204–214. https://doi.org/10.1016/j.geomorph.2014.06.017

Cattin, R., & Avouac, J. P. (2000). Modeling mountain building and the seismic cycle in the Himalaya of Nepal. *Journal of Geophysical Research: Solid Earth*, *105*(B6), 13389–13407. https://doi.org/10.1029/2000JB900032

Cordonnier, G., Bovy, B., & Braun, J. (2019). A versatile, linear complexity algorithm for flow routing in topographies with depressions. *Earth Surface Dynamics*, *7*(2), 549–562. https://doi.org/10.5194/esurf-7-549-2019

Croissant, T., & Braun, J. (2014). Constraining the stream power law: a novel approach combining a landscape evolution model and an inversion method. *Earth Surface Dynamics*, *2*(1), 155–166. https://doi.org/10.5194/esurf-2-155-2014

Dal Zilio, L., Hetényi, G., Hubbard, J., & Bollinger, L. (2021). Building the Himalaya from tectonic to earthquake scales. *Nature Reviews Earth & Environment*, *2*(4), 251–268. https://doi.org/10.1038/s43017-021-00143-1

Davy, P., & Lague, D. (2009). Fluvial erosion/transport equation of landscape evolution models revisited. *Journal of Geophysical Research: Earth Surface*, *114*(F3). https://doi.org/10.1029/2008JF001146

Densmore, A. L., Gupta, S., Allen, P. A., & Dawers, N. H. (2007). Transient landscapes at fault tips. *Journal of Geophysical Research*, *112*(F3), F03S08. https://doi.org/10.1029/2006JF000560

Ellis, M. A., & Barnes, J. B. (2015). A global perspective on the topographic response to fault growth. *Geosphere*, *11*(4), 1008–1023. https://doi.org/10.1130/GES01156.1

Faccenna, C., Glišović, P., Forte, A., Becker, T. W., Garzanti, E., Sembroni, A., & Gvirtzman, Z. (2019). Role of dynamic topography in sustaining the Nile River over 30 million years. *Nature Geoscience*, *12*(12), 1012–1017. https://doi.org/10.1038/s41561-019-0472-x

Farr, T. G., Rosen, P. A., Caro, E., Crippen, R., Duren, R., Hensley, S., et al. (2007). The Shuttle Radar Topography Mission. *Reviews of Geophysics*, *45*(2). https://doi.org/10.1029/2005RG000183

Fox, M., Goren, L., May, D. A., & Willett, S. D. (2014). Inversion of fluvial channels for paleorock uplift rates in Taiwan. *Journal of Geophysical Research: Earth Surface*, *119*(9), 1853–1875. https://doi.org/10.1002/2014JF003196

Gailleton, B., Sinclair, H. D., Mudd, S. M., Graf, E. L. S., & Mațenco, L. C. (2021). Isolating Lithologic Versus Tectonic Signals of River Profiles to Test Orogenic Models for the Eastern and Southeastern Carpathians. *Journal of Geophysical Research: Earth Surface*, *126*(8), e2020JF005970. https://doi.org/10.1029/2020JF005970

Gailleton, Boris, Mudd, S. M., Clubb, F. J., Grieve, S. W. D., & Hurst, M. D. (2021). Impact of Changing Concavity Indices on Channel Steepness and Divide Migration Metrics. *Journal of Geophysical Research: Earth Surface*, *126*(10), e2020JF006060. https://doi.org/10.1029/2020JF006060

Gailleton, Boris, Malatesta, L. C., Cordonnier, G., & Braun, J. (2024). CHONK 1.0: landscape evolution framework: cellular automata meets graph theory. *Geoscientific Model Development*, *17*(1), 71–90. https://doi.org/10.5194/gmd-17-71-2024

Godard, V., Bourles, D. L., Spinabella, F., Burbank, D. W., Bookhagen, B., Fisher, G. B., et al. (2014). Dominance of tectonics over climate in Himalayan denudation. *Geology*, *42*(3), 243–246. https://doi.org/10.1130/G35342.1

Goren, L., Fox, M., & Willett, S. D. (2014). Tectonics from fluvial topography using formal linear inversion: Theory and applications to the Inyo Mountains, California. *Journal of Geophysical Research: Earth Surface*, *119*(8), 1651–1681. https://doi.org/10.1002/2014JF003079

Goren, Liran, Fox, M., & Willett, S. D. (2022). Linear Inversion of Fluvial Long Profiles to Infer Tectonic Uplift Histories. In *Treatise on Geomorphology* (pp. 225–248). Elsevier. https://doi.org/10.1016/B978-0-12-818234-5.00075-4

Hack, J. T. (1973). *Stream-profile analysis and stream-gradient index*. U.S. Geological Survey.

Harel, M.-A., Mudd, S. M., & Attal, M. (2016). Global analysis of the stream power law parameters based on worldwide 10Be denudation rates. *Geomorphology*, *268*, 184–196. https://doi.org/10.1016/j.geomorph.2016.05.035

Hergarten, S., & Robl, J. (2022). The linear feedback precipitation model (LFPM 1.0) – a simple and efficient model for orographic precipitation in the context of landform evolution modeling. *Geoscientific Model Development*, *15*(5), 2063–2084. https://doi.org/10.5194/gmd-15-2063-2022

Herman, F., Copeland, P., Avouac, J.-P., Bollinger, L., Mahéo, G., Le Fort, P., et al. (2010). Exhumation, crustal deformation, and thermal structure of the Nepal Himalaya derived from the inversion of thermochronological and thermobarometric data and modeling of the topography. *Journal of Geophysical Research: Solid Earth*, *115*(B6). https://doi.org/10.1029/2008JB006126

Holtmann, R., Cattin, R., Simoes, M., & Steer, P. (2023). Revealing the hidden signature of fault slip history in the morphology of degrading scarps. *Scientific Reports*, *13*(1), 3856. https://doi.org/10.1038/s41598-023-30772-z

Howard, A. D., & Kerby, G. (1983). Channel changes in badlands. *GSA Bulletin*, *94*(6), 739–752. https://doi.org/10.1130/0016-7606(1983)94<739:CCIB>2.0.CO;2

Huffman, G. J., Bolvin, D. T., Braithwaite, D., Hsu, K., Joyce, R., Xie, P., & Yoo, S.-H. (2015). NASA global precipitation measurement (GPM) integrated multi-satellite retrievals for GPM (IMERG). *Algorithm Theoretical Basis Document (ATBD) Version*, *4*(26), 30.

Jackson, M., & Bilham, R. (1994). Constraints on Himalayan deformation inferred from vertical velocity fields in Nepal and Tibet. *Journal of Geophysical Research: Solid Earth*, *99*(B7), 13897–13912. https://doi.org/10.1029/94JB00714

Jolivet, R., Simons, M., Duputel, Z., Olive, J., Bhat, H. S., & Bletery, Q. (2020). Interseismic loading of subduction megathrust drives long term uplift in northern Chile, 1–21. https://doi.org/10.1029/2019GL085377

King, G. C. P., Stein, R. S., & Rundle, J. B. (1988). The Growth of Geological Structures by Repeated Earthquakes 1. Conceptual Framework. *Journal of Geophysical Research: Solid Earth*, *93*(B11), 13307–13318. https://doi.org/10.1029/JB093iB11p13307

Kirby, E., & Whipple, K. X. (2012). Expression of active tectonics in erosional landscapes. *Journal of Structural Geology*, *44*, 54–75. https://doi.org/10.1016/j.jsg.2012.07.009

Lavé, J., & Avouac, J. P. (2001). Fluvial incision and tectonic uplift across the Himalayas of central Nepal. *Journal of Geophysical Research: Solid Earth*, *106*(B11), 26561–26591. https://doi.org/10.1029/2001JB000359

Leonard, J. S., & Whipple, K. X. (2021). Influence of Spatial Rainfall Gradients on River Longitudinal Profiles and the Topographic Expression of Spatially and Temporally Variable Climates in Mountain Landscapes. *Journal of Geophysical Research: Earth Surface*, *126*(12), e2021JF006183. https://doi.org/10.1029/2021JF006183

Leonard, J. S., Whipple, K. X., & Heimsath, A. M. (2023). Isolating climatic, tectonic, and lithologic controls on mountain landscape evolution. *Science Advances*, *9*(3), eadd8915. https://doi.org/10.1126/sciadv.add8915

Lindsey, E. O., Almeida, R., Mallick, R., Hubbard, J., Bradley, K., Tsang, L. L. H., et al. (2018). Structural Control on Downdip Locking Extent of the Himalayan Megathrust. *Journal of Geophysical Research: Solid Earth*, *123*(6), 5265–5278. https://doi.org/10.1029/2018JB015868

Malatesta, L. C., Bruhat, L., Finnegan, N. J., & Olive, J.-A. L. (2021). Co-location of the Downdip End of Seismic Coupling and the Continental Shelf Break. *Journal of Geophysical Research: Solid Earth*, *126*(1), e2020JB019589. https://doi.org/10.1029/2020JB019589

Matsuoka, N. (1998). The relationship between frost heave and downslope soil movement: field measurements in the Japanese Alps. *Permafrost and Periglacial Processes*, *9*(2), 121–133. https://doi.org/10.1002/(SICI)1099-1530(199804/06)9:2<121::AID-PPP281>3.0.CO;2-C

Meade, B. J. (2010). The signature of an unbalanced earthquake cycle in Himalayan topography? *Geology*, *38*(11), 987–990. https://doi.org/10.1130/G31439.1

Merritt, W. S., Letcher, R. A., & Jakeman, A. J. (2003). A review of erosion and sediment transport models. *Environmental Modelling & Software*, *18*(8), 761–799. https://doi.org/10.1016/S1364-8152(03)00078-1

Molnar, P., & England, P. (1990). Late Cenozoic uplift of mountain ranges and global climate change: chicken or egg? *Nature*, *346*(6279), 29–34. https://doi.org/10.1038/346029a0

Mortimer, E., Kirstein, L. A., Stuart, F. M., & Strecker, M. R. (2016). Spatio-temporal trends in normal-fault segmentation recorded by low-temperature thermochronology: Livingstone fault scarp, Malawi Rift, East African Rift System. *Earth and Planetary Science Letters*, *455*, 62–72. https://doi.org/10.1016/j.epsl.2016.08.040

Mudd, S. M., Attal, M., Milodowski, D. T., Grieve, S. W. D., & Valters, D. A. (2014). A statistical framework to quantify spatial variation in channel gradients using the integral method of channel profile analysis. *Journal of Geophysical Research: Earth Surface*, *119*(2), 138–152. https://doi.org/10.1002/2013JF002981

Nadai, A. (1963). Theory of flow and fracture of solids. *New York, NY: McGraw-Hill*. Retrieved from https://cir.nii.ac.jp/crid/1130282270243960576

O'Callaghan, J. F., & Mark, D. M. (1984). The extraction of drainage networks from digital elevation data. *Computer Vision, Graphics, and Image Processing*, *28*(3), 323–344. https://doi.org/10.1016/S0734-189X(84)80011-0

Olive, J.-A., & Behn, M. D. (2014). Rapid rotation of normal faults due to flexural stresses: An explanation for the global distribution of normal fault dips. *Journal of Geophysical Research: Solid Earth*, *119*(4), 3722–3739. https://doi.org/10.1002/2013JB010512

Olive, J.-A., Malatesta, L. C., Behn, M. D., & Buck, W. R. (2022). Sensitivity of rift tectonics to global variability in the efficiency of river erosion. *Proceedings of the National Academy of Sciences*, *119*(13), e2115077119. https://doi.org/10.1073/pnas.2115077119

Oryan, B., & Buck, W. R. (2020). Larger tsunamis from megathrust earthquakes where slab dip is reduced. *Nature Geoscience*. https://doi.org/10.1038/s41561-020-0553-x

Oryan, B., Betka, P. M., Steckler, M. S., Nooner, S. L., Lindsey, E. O., Mondal, D., et al. (2023). New GNSS and Geological Data From the Indo-Burman Subduction Zone Indicate Active Convergence on Both a Locked Megathrust and the Kabaw Fault. *Journal of Geophysical Research: Solid Earth*, *128*(4), e2022JB025550. https://doi.org/10.1029/2022JB025550

Oryan, B., Olive, J.-A., Jolivet, R., Malatesta, L. C., Gailleton, B., & Bruhat, L. (2024). Megathrust locking encoded in subduction landscapes. *Science Advances*, *10*(17), eadl4286. https://doi.org/10.1126/sciadv.adl4286

Perron, J. T., & Royden, L. (2013). An integral approach to bedrock river profile analysis. *Earth Surface Processes and Landforms*, *38*(6), 570–576. https://doi.org/10.1002/esp.3302

Ponza, A., Pazzaglia, F. J., & Picotti, V. (2010). Thrust-fold activity at the mountain front of the Northern Apennines (Italy) from quantitative landscape analysis. *Geomorphology*, *123*(3), 211–231. https://doi.org/10.1016/j.geomorph.2010.06.008

Pritchard, D., Roberts, G. G., White, N. J., & Richardson, C. N. (2009). Uplift histories from river profiles. *Geophysical Research Letters*, *36*(24). https://doi.org/10.1029/2009GL040928

Robert, X., van der Beek, P., Braun, J., Perry, C., Dubille, M., & Mugnier, J.-L. (2009). Assessing Quaternary reactivation of the Main Central thrust zone (central Nepal Himalaya): New thermochronologic data and numerical modeling. *Geology*, *37*(8), 731–734. https://doi.org/10.1130/G25736A.1

Roberts, G. P., & Michetti, A. M. (2004). Spatial and temporal variations in growth rates along active normal fault systems: an example from The Lazio–Abruzzo Apennines, central Italy. *Journal of Structural Geology*, *26*(2), 339–376. https://doi.org/10.1016/S0191-8141(03)00103-2

Roering, J. J., Kirchner, J. W., & Dietrich, W. E. (1999). Evidence for nonlinear, diffusive sediment transport on hillslopes and implications for landscape morphology. *Water Resources Research*, *35*(3), 853–870. https://doi.org/10.1029/1998WR900090

Roering, J. J., Kirchner, J. W., Sklar, L. S., & Dietrich, W. E. (2001). Hillslope evolution by nonlinear creep and landsliding: An experimental study. *Geology*, *29*(2), 143. https://doi.org/10.1130/0091-7613(2001)029<0143:HEBNCA>2.0.CO;2

Rosenbloom, N. A., & Anderson, R. S. (1994). Hillslope and channel evolution in a marine terraced landscape, Santa Cruz, California. *Journal of Geophysical Research: Solid Earth*, *99*(B7), 14013–14029. https://doi.org/10.1029/94JB00048

Saillard, M., Audin, L., Rousset, B., Avouac, J.-P., Chlieh, M., Hall, S. R., et al. (2017). From the seismic cycle to long-term deformation: linking seismic coupling and Quaternary coastal geomorphology along the Andean megathrust. *Tectonics*, *36*(2), 241–256. https://doi.org/10.1002/2016TC004156

Smith, A. G. G., Fox, M., Moore, J. R., Miller, S. R., Goren, L., Morriss, M. C., & Carter, A. (2024). One Million Years of Climate-Driven Rock Uplift Rate Variation on the Wasatch Fault

Revealed by Fluvial Topography. *American Journal of Science*, *324*. https://doi.org/10.2475/001c.92194

Snyder, N. P., Whipple, K. X., Tucker, G. E., & Merritts, D. J. (2000). Landscape response to tectonic forcing: Digital elevation model analysis of stream profiles in the Mendocino triple junction region, northern California. *GSA Bulletin*, *112*(8), 1250–1263. https://doi.org/10.1130/0016-7606(2000)112<1250:LRTTFD>2.0.CO;2

Sreejith, K. M., Sunil, P. S., Agrawal, R., Saji, A. P., Rajawat, A. S., & Ramesh, D. S. (2018). Audit of stored strain energy and extent of future earthquake rupture in central Himalaya. *Scientific Reports*, *8*(1), 16697. https://doi.org/10.1038/s41598-018-35025-y

Steckler, M. S., Mondal, D. R., Akhter, S. H., Seeber, L., Feng, L., Gale, J., et al. (2016). Locked and loading megathrust linked to active subduction beneath the Indo-Burman Ranges. *Nature Geoscience*, *9*(8), 615–618. https://doi.org/10.1038/ngeo2760

Su, Q., Xie, H., Yuan, D.-Y., & Zhang, H.-P. (2017). Along-strike topographic variation of Qinghai Nanshan and its significance for landscape evolution in the northeastern Tibetan Plateau. *Journal of Asian Earth Sciences*, *147*, 226–239. https://doi.org/10.1016/j.jseaes.2017.07.019

Tarantola, A. (2005). *Inverse Problem Theory and Methods for Model Parameter Estimation*. Society for Industrial and Applied Mathematics. https://doi.org/10.1137/1.9780898717921

Taylor, W. J., & Switzer, D. D. (2001). Temporal changes in fault strike (to 90°) and extension directions during multiple episodes of extension: An example from eastern Nevada. *GSA*

Bulletin, *113*(6), 743–759. https://doi.org/10.1130/0016-7606(2001)113<0743:TCIFST>2.0.CO;2

Watts, A. B. (2001). *Isostasy and Flexure of the Lithosphere*. Cambridge University Press. Retrieved from https://books.google.com/books?hl=en&lr=&id=QlUgBqJ6m-MC&oi=fnd&pg=PR11&dq=isostasy&ots=KMIwT-K-82&sig=EEBiI2c-910Do0N-5fBIxEyOtq8

Weissel, J. K., & Karner, G. D. (1989). Flexural uplift of rift flanks due to mechanical unloading of the lithosphere during extension. *Journal of Geophysical Research: Solid Earth*, *94*(B10), 13919–13950. https://doi.org/10.1029/JB094iB10p13919

Whipple, K. X. (2009). The influence of climate on the tectonic evolution of mountain belts. *Nature Geoscience*, *2*(2), 97–104. https://doi.org/10.1038/ngeo413

Whipple, K. X., & Tucker, G. E. (1999). Dynamics of the stream-power river incision model: Implications for height limits of mountain ranges, landscape response timescales, and research needs. *Journal of Geophysical Research: Solid Earth*, *104*(B8), 17661–17674. https://doi.org/10.1029/1999JB900120

Willgoose, G., Bras, R. L., & Rodriguez-Iturbe, I. (1991). A physical explanation of an observed link area-slope relationship. *Water Resources Research*, *27*(7), 1697–1702. https://doi.org/10.1029/91WR00937

Williams, P. L., & Cole, J. C. (2007). *Geologic Map of the Albuquerque 30′ X 60′ Quadrangle, North-central New Mexico* (Vol. 2946). US Department of the Interior, US Geological Survey. Retrieved from https://books.google.com/books?hl=en&lr=&id=SmHuAAAAMAAJ&oi=fnd&pg=PA1&dq

=Geologic+Map+of+the+Albuquerque+30%E2%80%99+x+60%E2%80%99+Quadrangle,+North-Central+New+Mexico&ots=XjNI3pAW57&sig=zlxdaGIePxXrpviuYPt1dkoxExo

Wobus, C., Whipple, K. X., Kirby, E., Snyder, N., Johnson, J., Spyropolou, K., et al. (2006). Tectonics from topography: Procedures, promise, and pitfalls. In S. D. Willett, N. Hovius, M. T. Brandon, & D. M. Fisher (Eds.), *Tectonics, Climate, and Landscape Evolution* (Vol. 398, p. 0). Geological Society of America. https://doi.org/10.1130/2006.2398(04)

Yanites, B. J., Tucker, G. E., Mueller, K. J., Chen, Y.-G., Wilcox, T., Huang, S.-Y., & Shi, K.-W. (2010). Incision and channel morphology across active structures along the Peikang River, central Taiwan: Implications for the importance of channel width. *GSA Bulletin*, *122*(7–8), 1192–1208. https://doi.org/10.1130/B30035.1

9 Funding

This work was funded by the Emergence(s)–Ville de Paris Program Project “Inelasticity in the Subduction earthquake cycle” (J.-A.O.); the French Agence Nationale de la Recherche (ANR) grant GeoSigMA (J.-A.O.), the European Research Council (ERC) under the European Union’s horizon 2020 research and innovation program, Geo-4d project, grant agreement 758210 (R.J.); institut Universitaire de France (R.J.); h2020 european Research council, grant no. 803721 (B.G.); Chateaubriand Fellowship Program ,Green Postdoctoral Scholarship from IGPP at SiO and national Science Foundation, grant no. nSF-OAc- 2311208 (B.O.)

10 Supplementary information

Text S1 – B Splines

The B-spline function we used in parametrizing the uplift are described as follow (De Boor, 1978; Piegl & Tiller, 1997):

1. $U(x) = \sum_i^{i+d} Q_i B_{i,d}(x)$

Where Q_i is the spline coefficient controlling the behavior of the B-spline basis function of order d, $B_{i,d}$ (x), defined recursively in the following way:

2. $B_{i,0}(x) = \begin{cases} 1, & x \in [t_i, t_{i+1}] \\ 0, & elsewhere \end{cases}$

$$B_{i,d}(x) = \frac{x - t_i}{t_{i+d} - t_i} B_{i,d-1}(x) + \frac{t_{i+d+1} - x}{t_{i+d+1} - t_{i+1}} B_{i+1,d-1}(x)$$

t_i is the position of node i.

To describe a two-dimensional uplift patterns we rely on a convolution of B-spline basis function to describe a surface (De Boor, 1978; Piegl & Tiller, 1997):

3. $U(x, y) = \sum_i^{n+d} \sum_j^{j+d} Q_{i,j} B_{i,d}(x) B_{j,d}(y)$

To compute our uplift function, we distribute nodes along a rectangle uniform grid with constant spacing along the x and y axis. This enables us to adopt a simpler and computationally efficient form of B-spline basis (Agrapart & Batailly, 2020). For 1D cubic solution where uplift varies along the x-axis we use:

4. $U(x) = \frac{1}{6} [u_i^3 \; u_i^2 \; u_i \; 1] \cdot R \cdot \begin{bmatrix} Q_i \\ Q_{i+1} \\ Q_{i+2} \\ Q_{i+3} \end{bmatrix}$

For the 2D case where uplift pattern is a function of x and y we use:

$$5.\quad U(x,y) = \frac{1}{36}\left[v_j^3\ v_j^2\ v_j\ 1\right] \cdot R \cdot \begin{bmatrix} Q_{i,j} & Q_{i+1,j} & Q_{i+2,j} & Q_{i+3,j} \\ Q_{i,j+1} & Q_{i+1,j+1} & Q_{i+2,j+1} & Q_{i+3,j+1} \\ Q_{i,j+2} & Q_{i+1,j+2} & Q_{i+2,j+2} & Q_{i+3,j+2} \\ Q_{i,j+3} & Q_{i+1,j+3} & Q_{i+2,j+3} & Q_{i+3,j+3} \end{bmatrix} R^t \begin{bmatrix} \mu_i^3 \\ \mu_i^2 \\ \mu_i \\ 1 \end{bmatrix}$$

Where $\mu_i = \frac{x-t_i}{t_{i+1}-t_i}$, $v_j = \frac{y-t_j}{t_{j+1}-t_j}$ and $R = \begin{bmatrix} -1 & 3 & -3 & 1 \\ 3 & -6 & 3 & 0 \\ -3 & 0 & 3 & 0 \\ 1 & 4 & 1 & 0 \end{bmatrix}$.

We note that the numbers of parameters needed is nodes+d(=3) and as we are only interested in the shape of uplift and normalize our uplift solution between 0 and 1.

Finally, we highlight that our recovered uplift is constrained only by river nodes within our rectangular domain defining the b-spline surface. Nonetheless, we can extrapolate the uplift surface across the entire B-spline domain using these parameters. We consider that the recovered uplift applies only to the basins that feed our selected river nodes, as the water flowing through these influence the information they provide.

Cases	x_0 [km]	y_0 [km]	σ_x [km]	σ_y [km]	θ []	Illustration Fig.
Detachment limited, Sediment transportation, Hillslope diffusion (Fig. 1 ,2 and 3)	50	50	30	20	45	1,S2A
Temporal uplift shape (South ridge uplift function ; Fig 5)	50	70	100	40	0	S2B
Temporal change (North ridge uplift function ; Fig 5)	50	30	100	40	0	S2C
Climatic effect & Temporal uplift rate (Figs. 5 & 3)	50	50	1000	20	0	S2D
Erodibility ratio (Fig 6)	50	50	40	25	0	S2E

Table S1 – Imposed tectonic uplift used in synthetic landscape. Uplift functions illustrations are shown in Fig. S1.

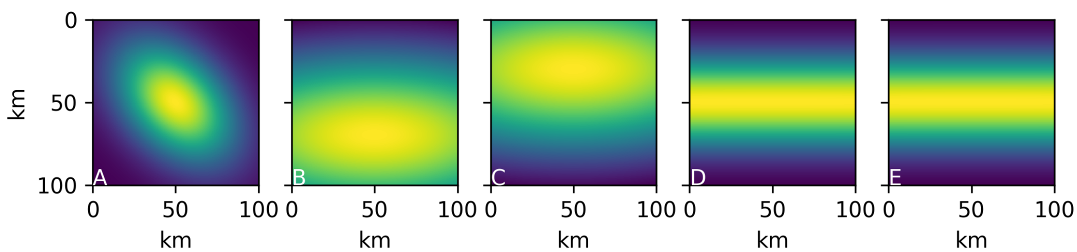

Fig S1 – Uplift imposed for synthetic landscapes cases (see table S1).

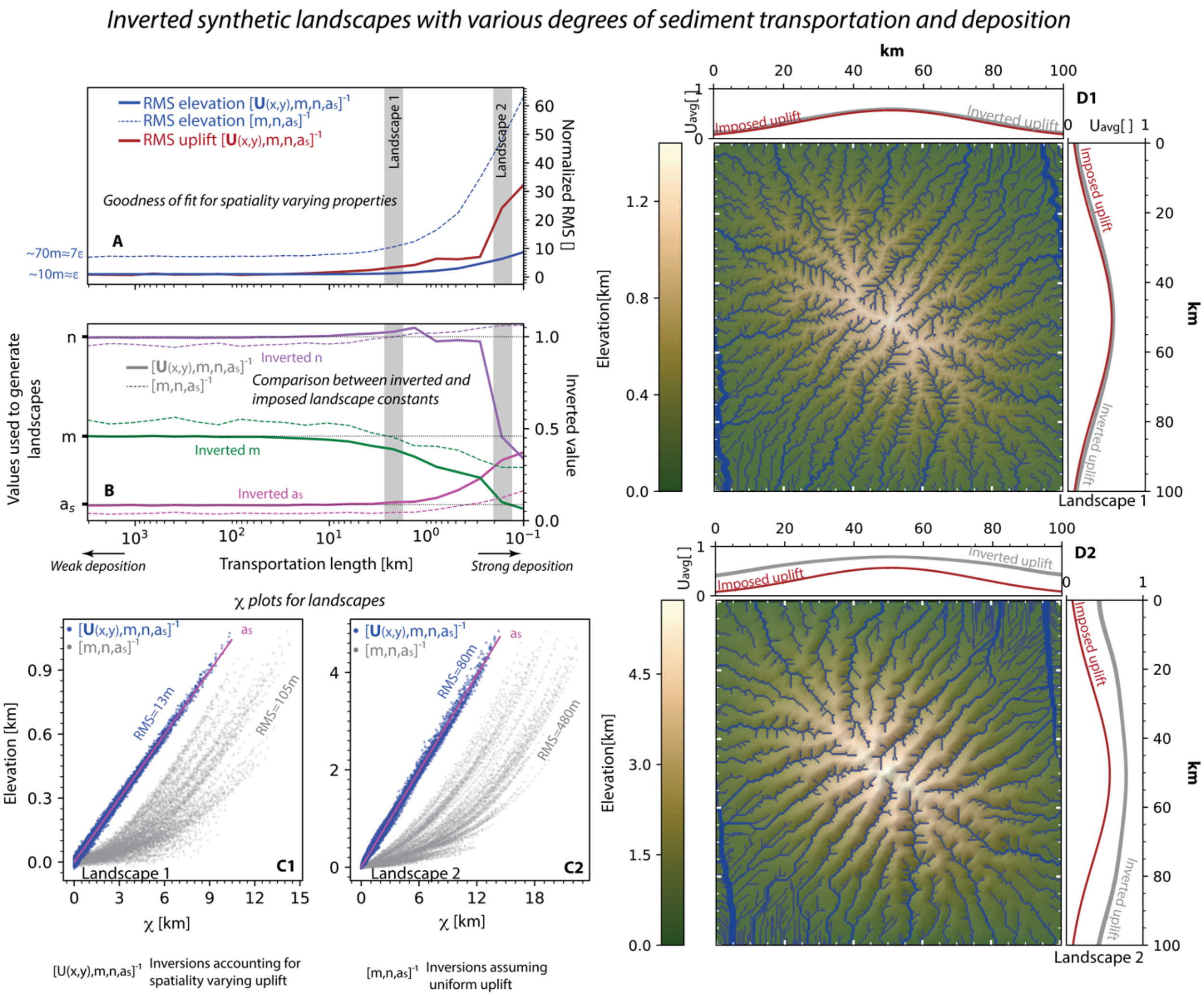

Figure S2 – Inverted synthetic landscapes with various degrees of sediment transportation and deposition. Panels A and B show comparison between imposed and recovered landscape properties for inversions of 50 synthetic landscapes, each characterized by a distinct simulated deposition value. A – RMS values for elevation and uplift and normalized with respect to value obtained for the landscape with the weakest deposition. ε denote error we introduced amounting to 10m (See section 4.2). B – Comparison between imposed (black dash curve) and mean inverted and $m, n\ and\ a_s$ values. Continuous and dashed curves denote inversion results including and excluding uplift, respectively. Grey vertical lines show two landscapes described in panels C and D. C – Points show elevation for 8000 river nodes and χ values derived from best inverted solution. Blue and grey denote inversion results including and excluding uplift, respectively. D – Landscapes Elevation. Blue dots show 8000 river nodes used for the inversion with dot size proportional to the drainage area. Marginal plots show average uplift along axis. Imposed uplift is shown in red curve and 500 samples randomly drawn from the inverted uplift posterior distribution and extrapolated to the domain are shown in grey.

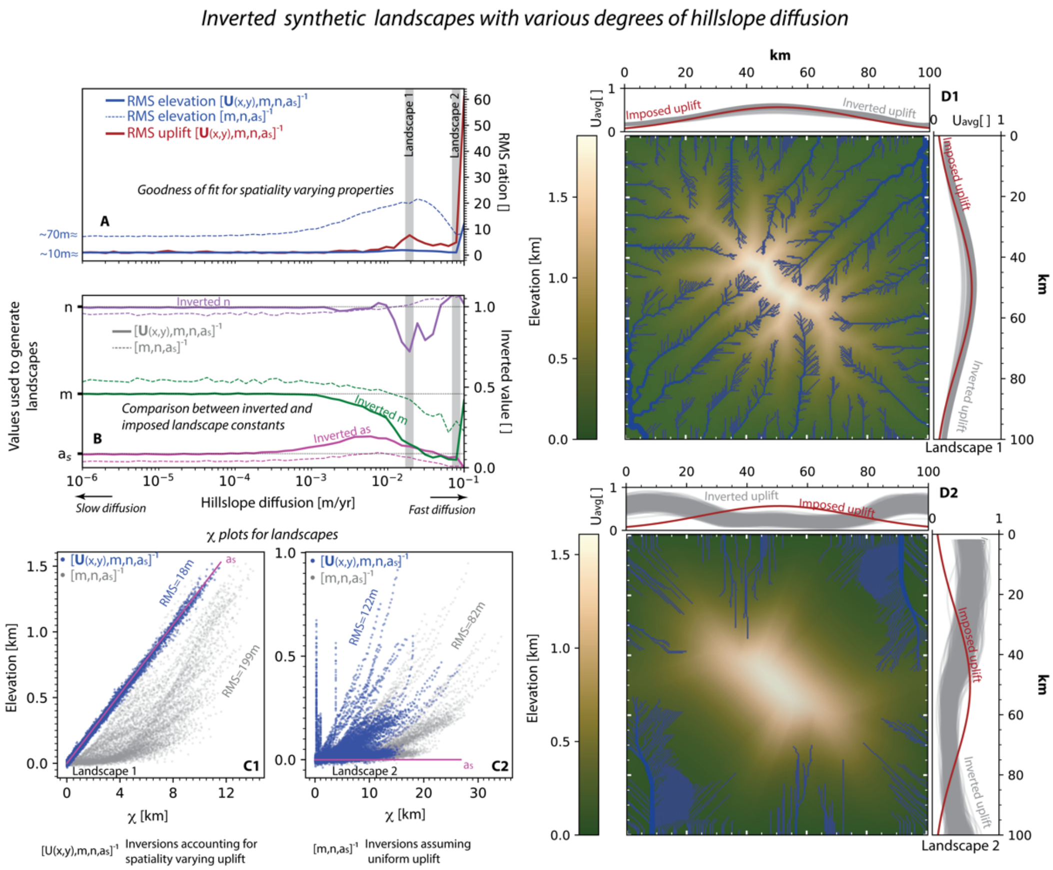

Figure S3 – Inverted synthetic landscapes with various degrees of hillslope diffusion. Panels A,A*,B and B* show comparison between imposed and recovered landscape properties for inversions of 50 synthetic landscapes, each characterized by a distinct h_o(See section 4.3.5). Panels with and without an * show outputs for inversions including and excluding the effect of orographic perception on drainage area, respectively. Blue curves in marginal plots in panels D1 and D2 show the averaged perception along the x axis where 1 and 0 indicate large and negligible perception, respectively.   See Fig. S2 for complete figure description.

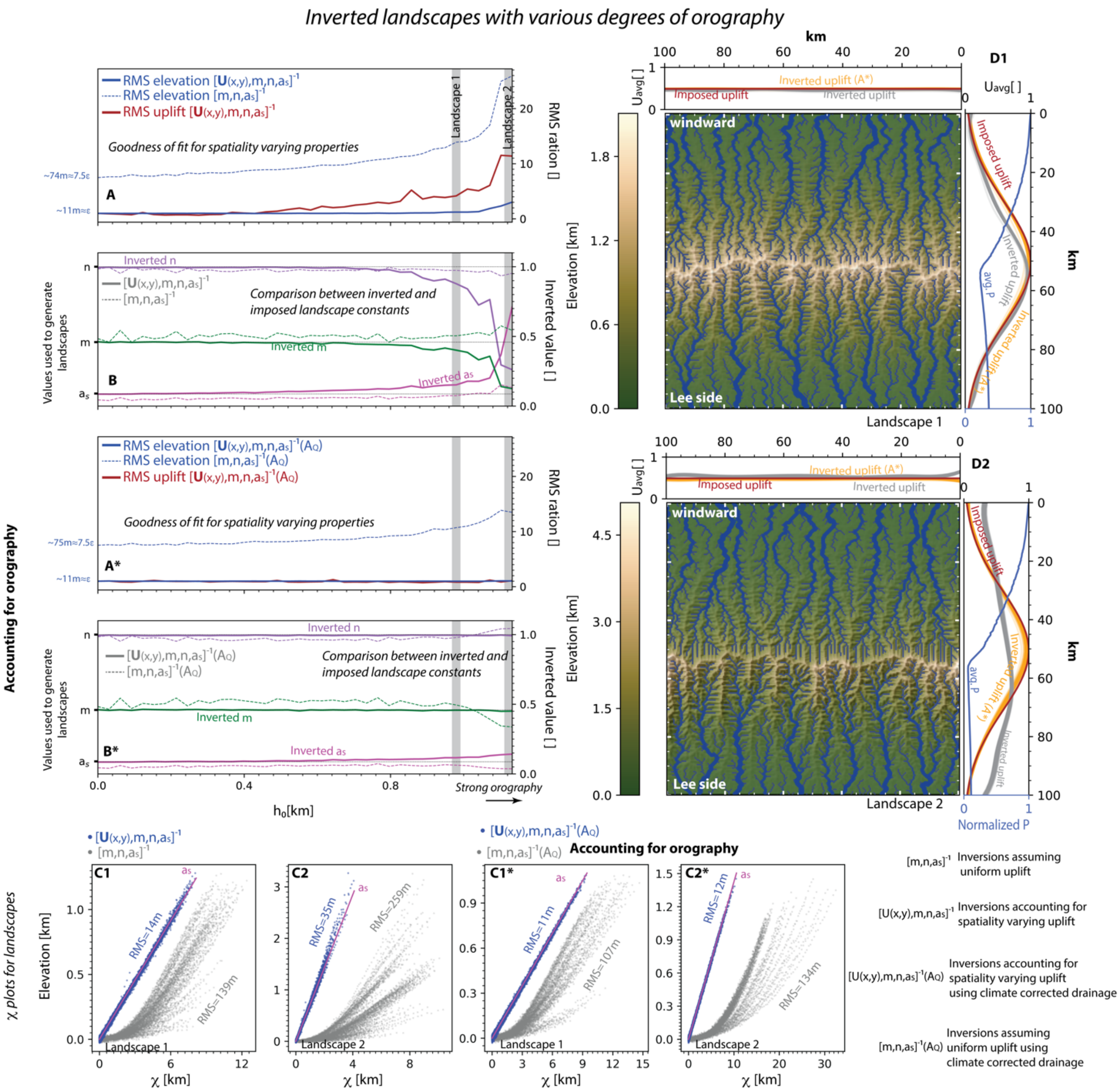

Figure S4 – Inverted synthetic landscapes with various degrees of orographic effect. Panels A,A*,B and B* show comparison between imposed and recovered landscape properties for inversions of 50 synthetic landscapes, each characterized by a distinct h_o(See section 4.3.5). Panels with and without an * show outputs for inversions including and excluding the effect of orographic perception on drainage area, respectively. Blue curves in marginal plots in panels D1 and D2 show the averaged perception along the x axis where 1 and 0 indicate large and negligible perception, respectively. See Fig. S2 for complete figure description.

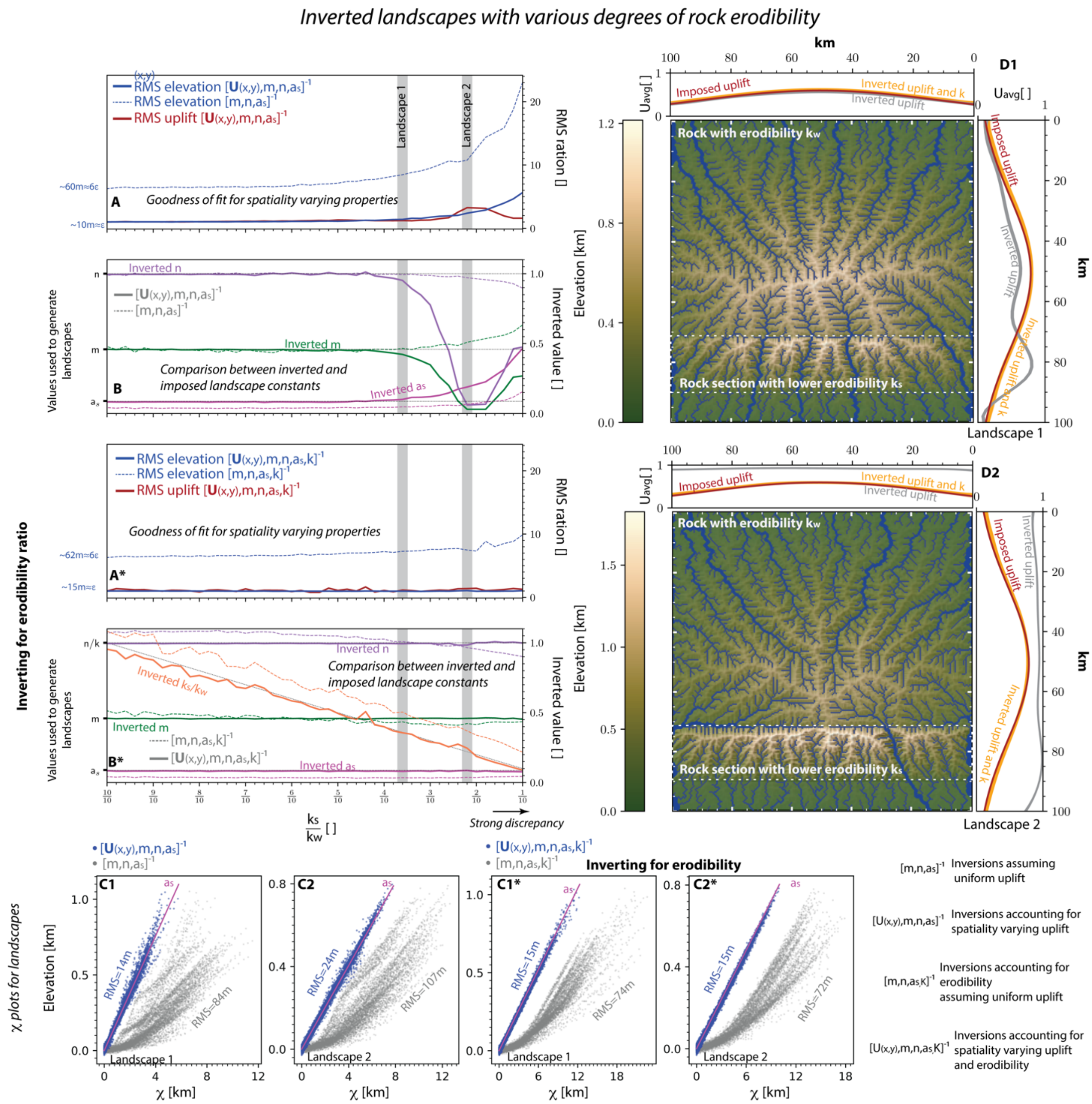

Figure S5 – Inverted synthetic landscapes with various degrees of rock erodibility. Panels A,A*,B and B* show comparison between imposed and recovered landscape properties for inversions of 50 synthetic landscapes, each characterized by a 20km wide section with a distinct erodibility value k_s. White dash line in D1 and D2 mark section characterized by erodibility of k_s. Panels with and without an * show outputs for inversions including and excluding erodibility, respectively. See Fig. S2 for complete figure description.

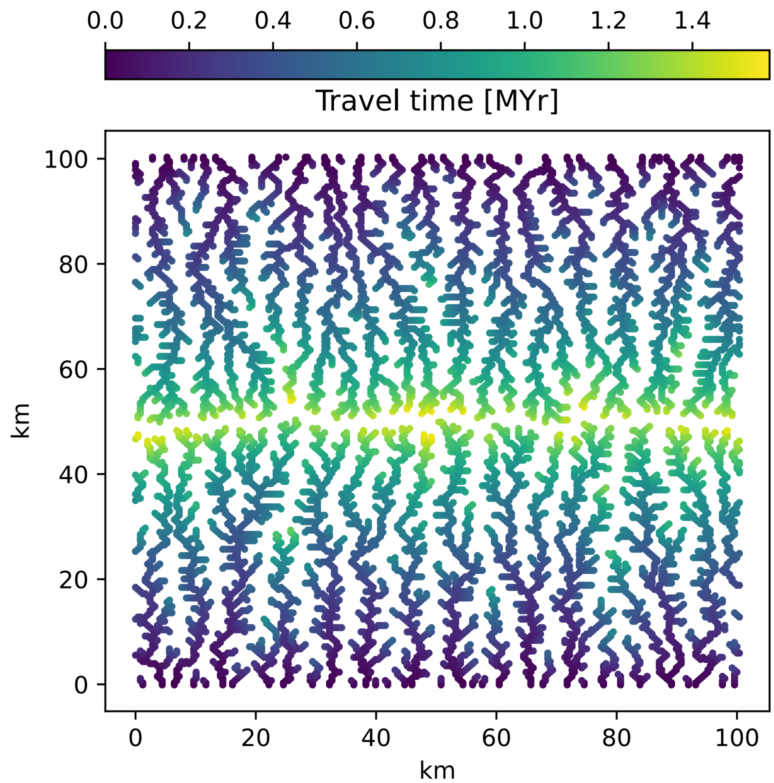

Fig S6– knickpoint travel time from base level to river node.

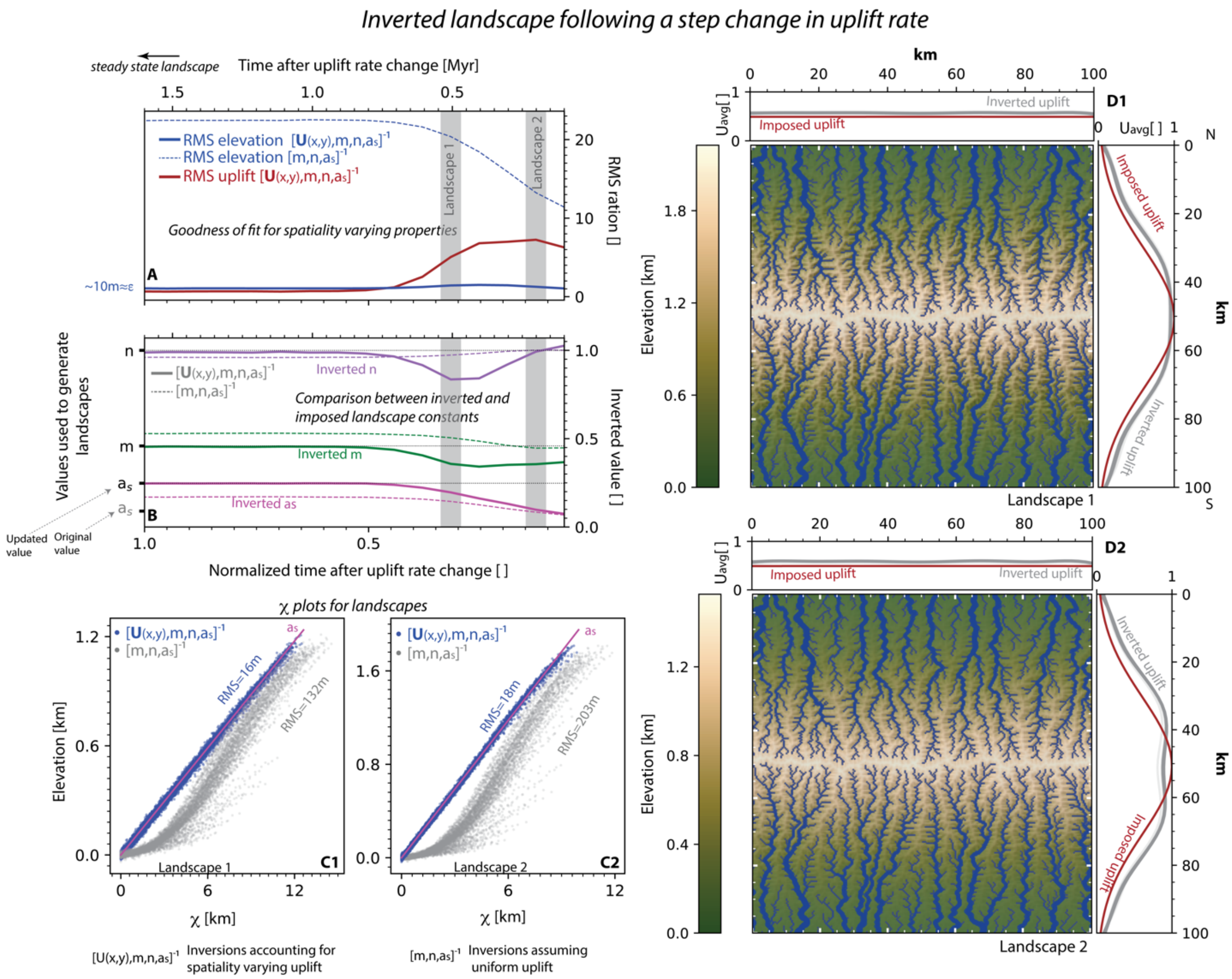

Figure S7 – Inverted synthetic landscape following an instantaneous change in uplift rate. Panels A and B show comparison between imposed and recovered landscape properties for inversions of snapshots of the landscape at intervals of 0.1 Myr following the step change. Results are presented in time normalized with respect to the duration the landscape requires to reach steady state. See Fig. S2 for complete figure description.

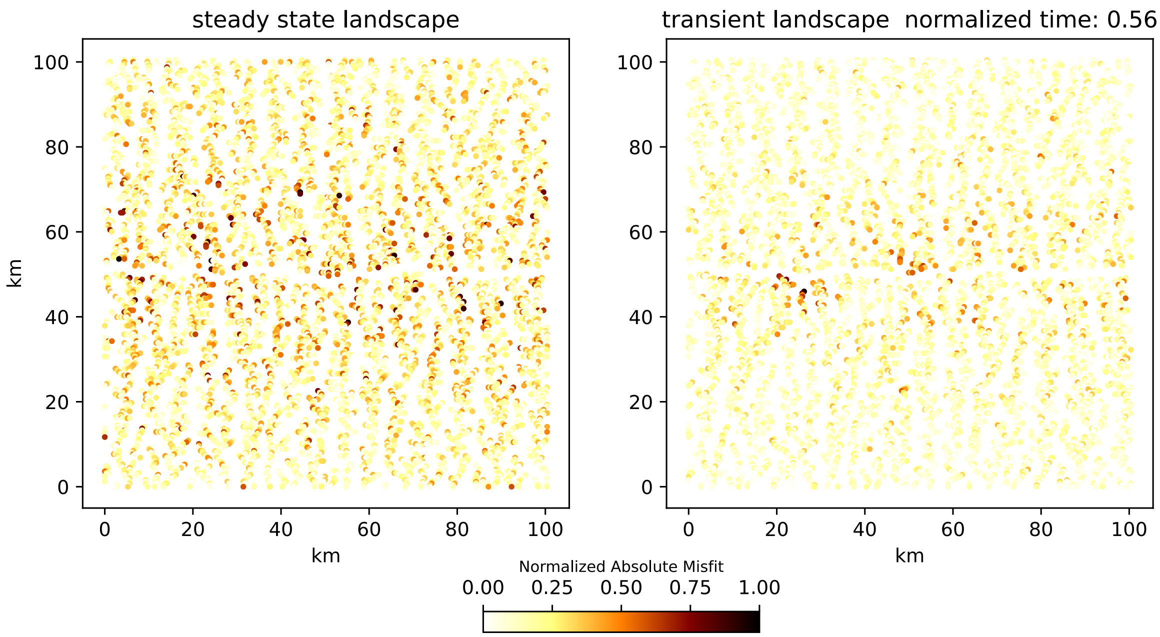

Fig S8 – Elevation misfit for two synthetic landscapes. The largest misfit values for the transient landscape are concentrated upstream around the river tips, which have not yet reached equilibrium. In contrast misfits are almost evenly distributed across steady state landscape.

Text S2 – Synthetic landscape subject to temporal changes in uplift pattern

For completeness we examine the effect of temporal changes in uplift pattern (under constant uplift rate) and simulate a detachment-limited landscape in equilibrium, characterized by a well-formed east-west mountain range along the southern end of the domain (Fig. 5; Table S1; Fig. S1). We then introduce a step change in the uplift pattern, resulting in a ~30 km slow migration of the mountain ridge towards the north (Fig. S9; Table S1; Fig. S1). Following this instantaneous change, we continue simulating the landscape for an additional 10 million years, performing inversions on landscape snapshots recorded at intervals of 0.1 million years.

Due to the nonlinearity and complexity of the signal we introduce (Royden & Taylor Perron, 2013; Steer, 2021), we estimate the time for the landscape to reach a new equilibrium by computing the mean of the absolute differences in topographic height across successive timesteps (green curve, Fig. S9A). Approximately 10 million years following the step change, the ridge stabilizes at its final position, with mean topographic change diminishing to about 1% of its maximum value post-change (Fig. S9A).

The inverted and recorded elevations align almost perfectly, while other landscape properties show more pronounced errors (Figs. S9A & S9B). This consistency in elevation retrieval suggests that the inversion effectively compensates with adjustments in other parameters to return accurate elevation values. This is because the transient signals are primarily driven by detachment-limited processes, in contrast to sediment deposition and hillslope diffusion. This illustrates the challenge of determining whether a natural landscape, lacking direct constraints on uplift and landscape constants, is in steady state based solely on elevation errors. Additional similarity with scenario (1) is that the recovered uplift almost perfectly matches the imposed uplift by about half the dimensionless time, significantly earlier than when the landscape reaches its final equilibrium. This is particularly notable given that the ridge still needs to migrate approximately 10 km before reaching its steady state position (Figs. S9D1 & S9D2).

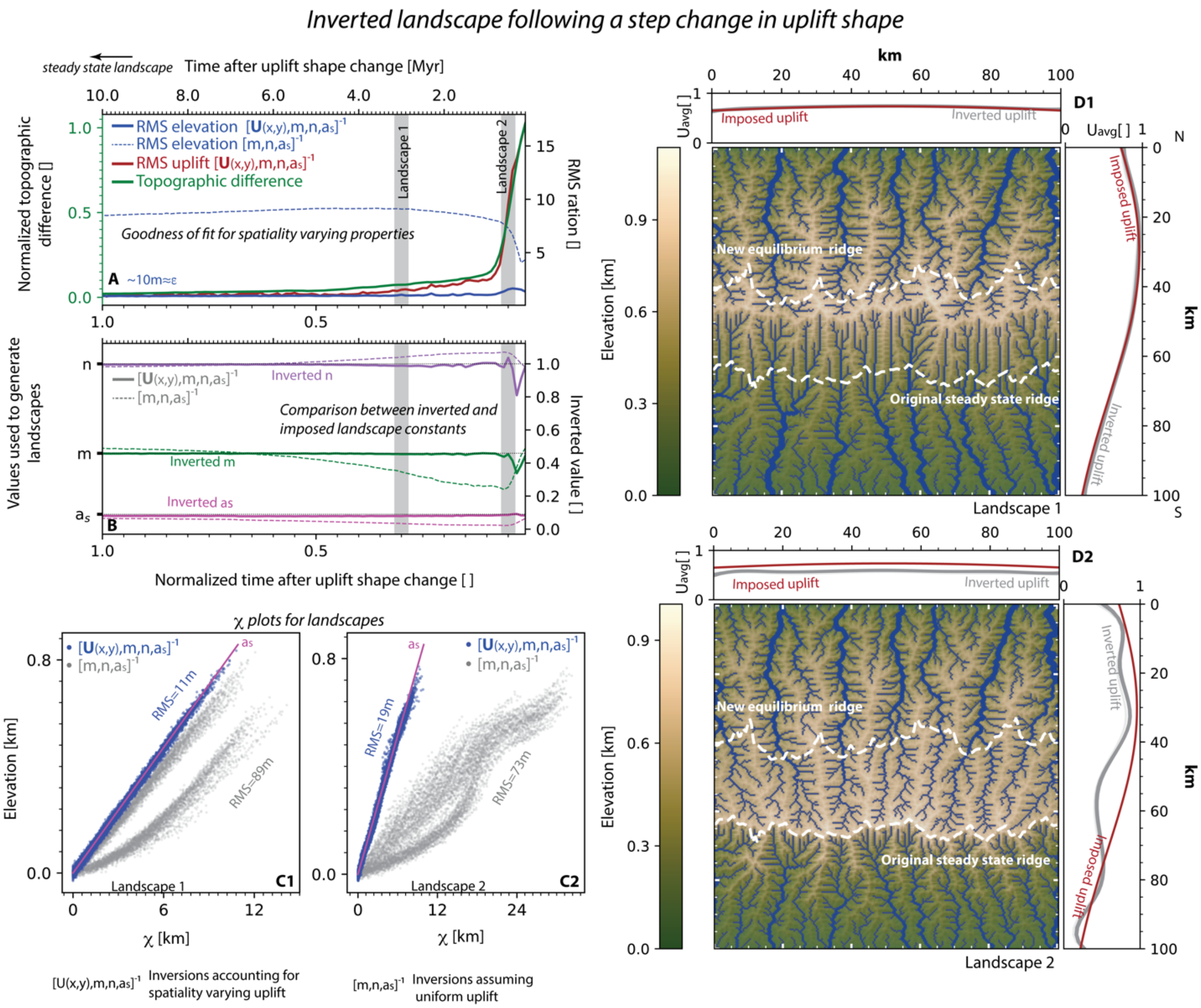

Figure S9 – Inverted synthetic landscape following an instantaneous change in uplift shape. Panels A and B show comparison between imposed and recovered landscape properties for inversions of snapshots of the landscape at intervals of 0.1 Myr following the step change. Results are presented in time normalized with respect to the duration the landscape requires to reach steady state. Green curve shows the normalized mean topographic difference computed between successive timesteps. Dashed white lines show the original and new positions of the ridge in steady state. See Fig. 2 for complete figure description.

Table S2 – Properties of natural landscapes. *Olive et al., 2022 and references therein. **Ellis & Barnes, 2015 and references therein. ^ See text S5.

	Base altitude for χ [m]	Min drainage area $[km^2]$	Master fault UTM coordinates (x1, y1) and (x2, y2) (m) + UTM zone *	Knots Used for inversion	Brittle layer thickness[km]*	$u_0[\frac{mm}{yr}]$	Age of onset [Myr]
Paeroa Range, New Zealand (A)	400	2.5	(4.3843e5, 5.7567e6) (4.3115e5, 5.7487e6) UTM 60H	1	6-8	1.5**	1-0.9**
Sandia Mountains, New Mexico, USA (B)	2100	2	(3.6423e5, 3.8973e6) (3.6452e5, 3.8866e6) UTM 13N	1	7-10	0.14^	22^
Wassuk Range, Nevada, USA (C)	1500	1	(3.4679e5,4.2762e6) (3.4620e5,4.2968e6) UTM 11S	4	11-14	0.6**	15**
Kipengere Range / N.E. shores of Lake Malawi, Tanzania (D)	550	1	(6.1128e5, 8.9515e6) (6.6862e5, 8.8871e6) UTM 36L	7	32-37	0.12^	23^
Lemhi Range, Idaho, USA (E)	2200	3	(2.6519e5, 4.9486e6) (2.875e5, 4.9305e6) UTM 12T	Kx=2 ky=3	12-16	0.5**	6.5**
Himalayas	550	10	UTM 45N	Kx=9; ky=9			

Text S2 - Akaike Information Criterion

The Akaike Information Criterion is a method used in statistics to determine the relative quality of statistical models for a given set of data. It is calculated using the formula:

$$AIC = 2(k - \ln(L))$$

where k is the number of parameters in the model and L is the maximum value of the likelihood function for the model.

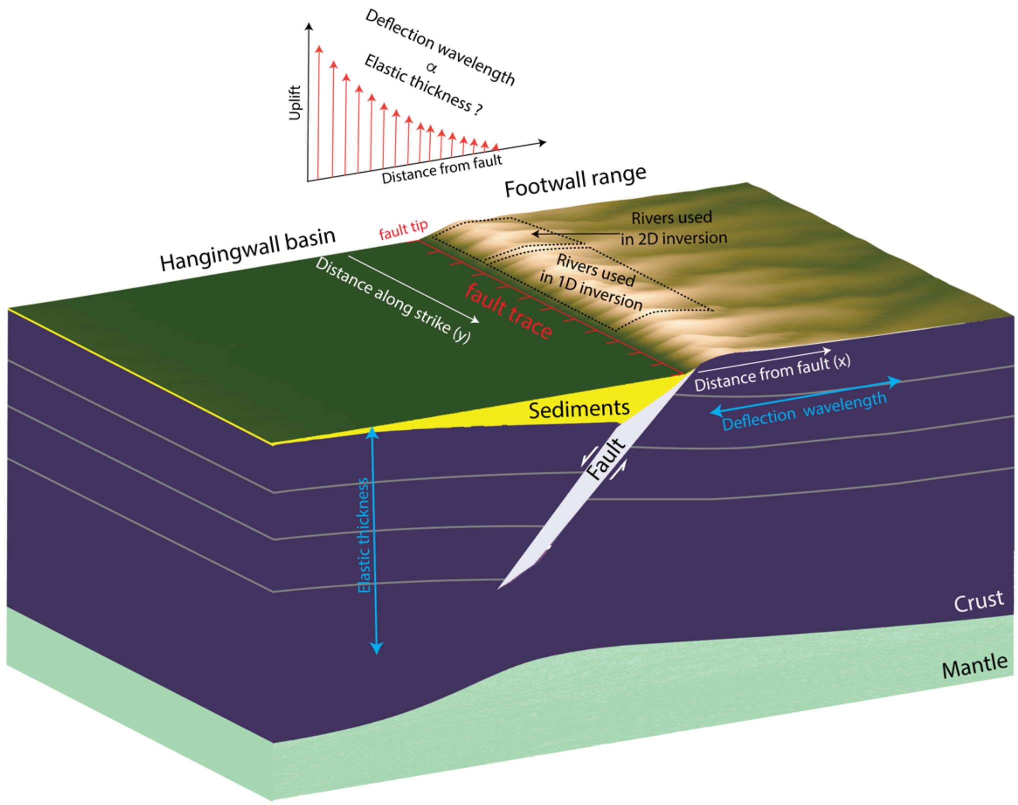

Figure S10 – Illustration showing the deflation of the lithosphere and resulting landscape due to offset accommodated along a half graben normal fault system.

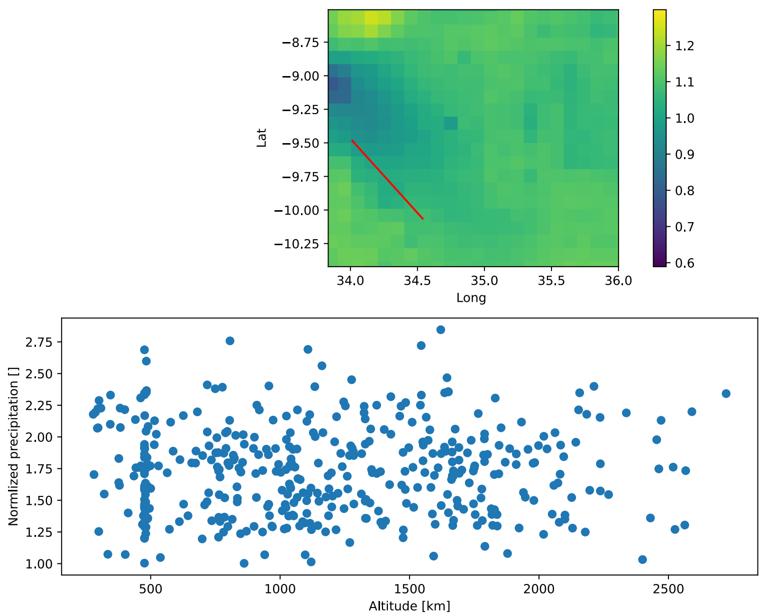

Fig S11 – Upper panel – Standard deviation of precipitation divided by the average precipitation per pixel for rainfall data collected over 23 years from November 1, 2000, by the GPM mission (Huffman et al., 2015). The red line indicates the position of the Livingston normal fault (Fig S8). Lower panel - Elevation and average precipitation for 418 data points corresponding to the rainfall data shown in the upper panel.

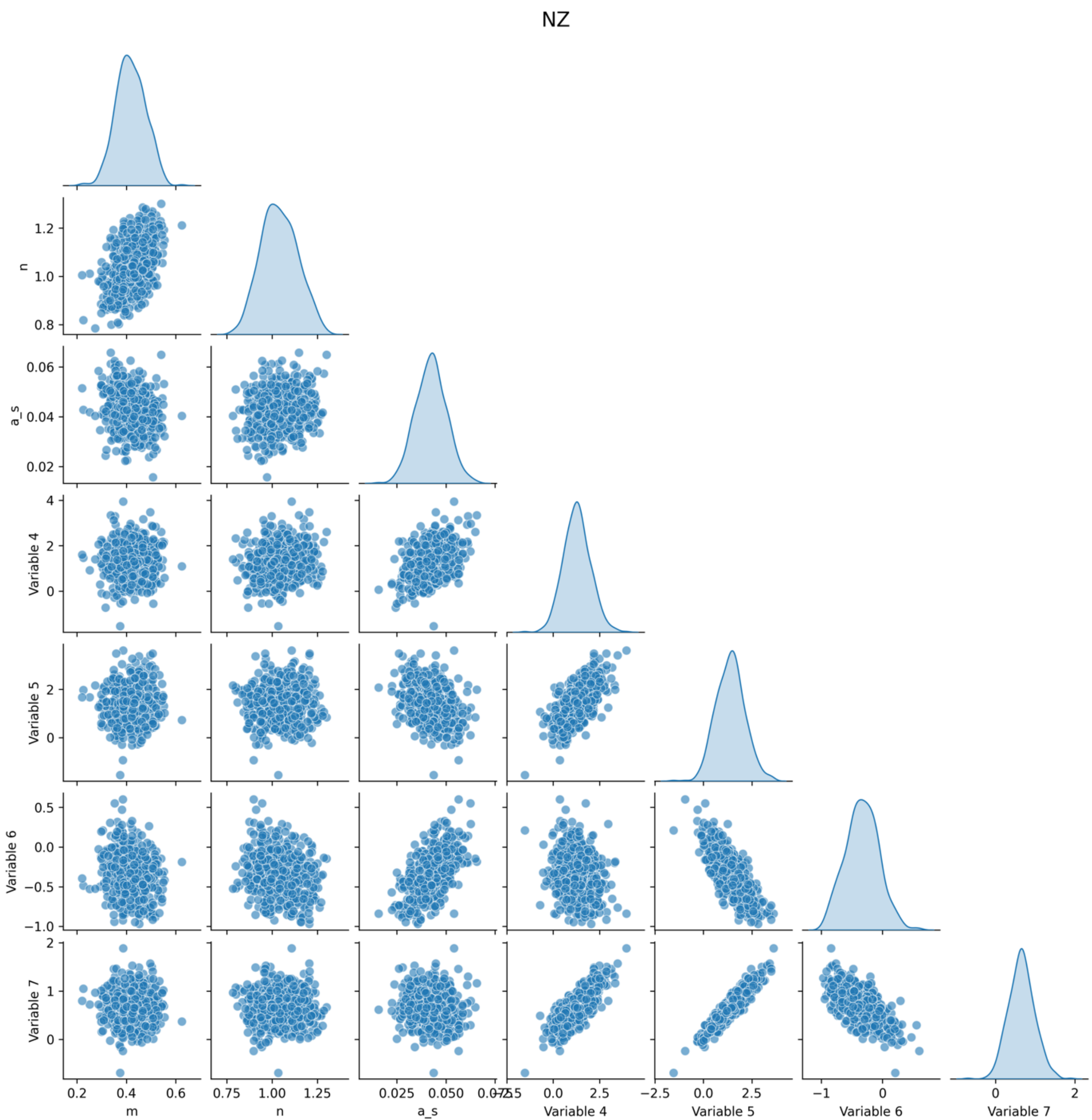

Figure S12 - Pair plots for the New Zeeland landscape. Variables 4-7 indicate parameters controlling the b-spline functions. These were estimated using 500 samples randomly drawn from the posterior distribution.

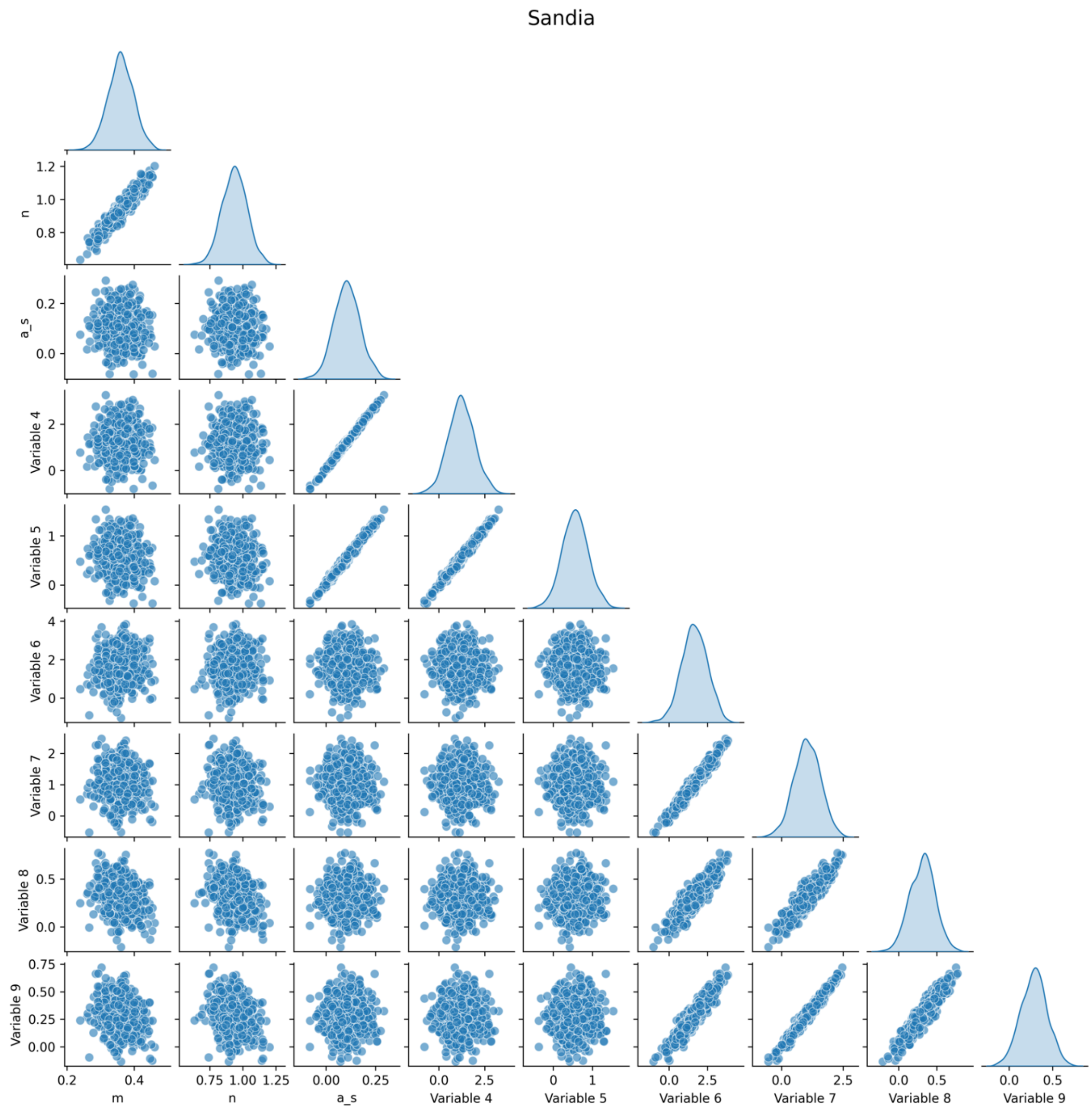

Figure S13 - Pair plots for the Sandia landscape. Variables 4-5 and 6-9 indicate parameters controlling the erodibility and b-spline functions, respectively. These were estimated using 500 samples randomly drawn from the posterior distribution.

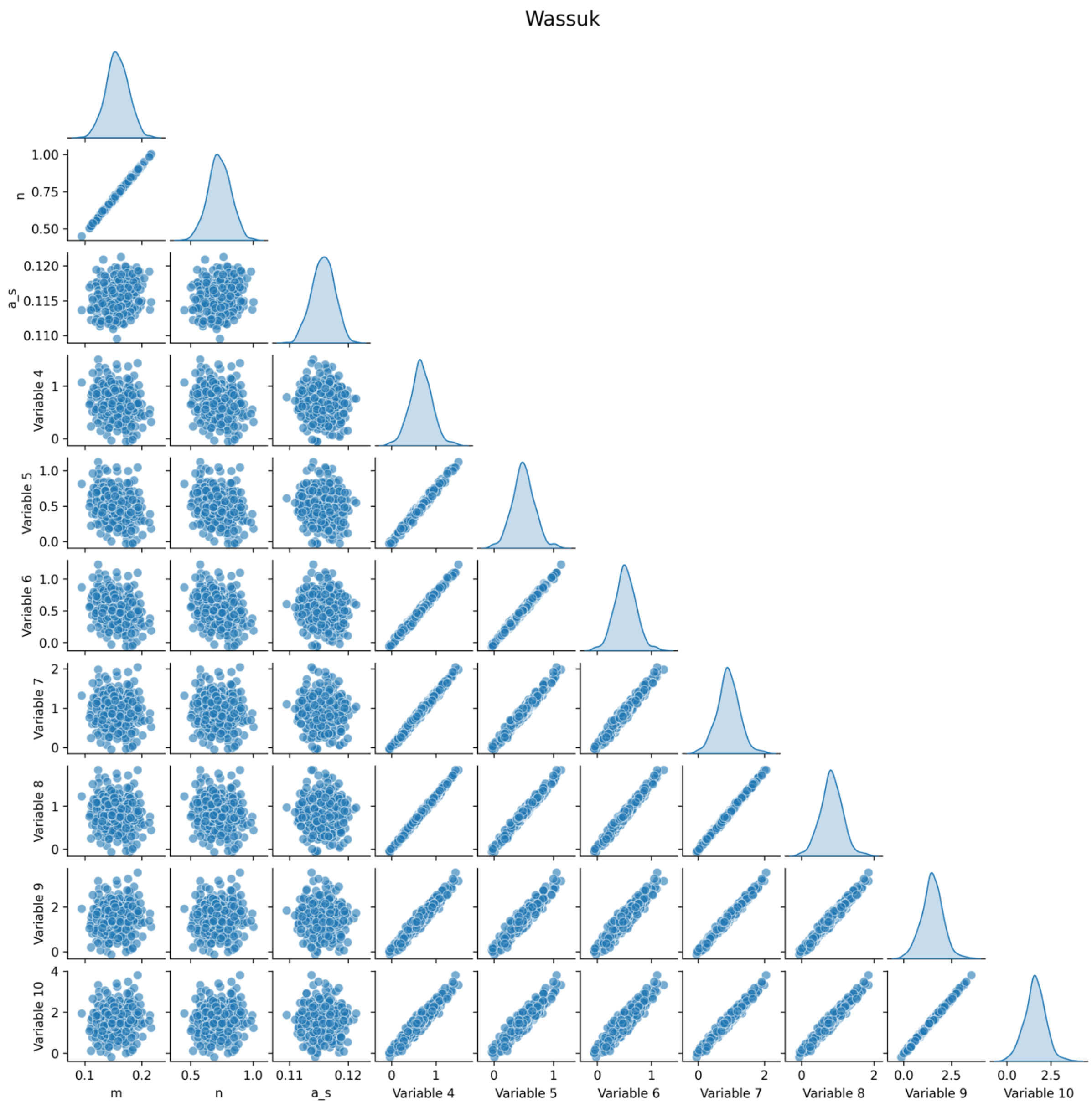

Figure S14 - Pair plots for the Wassuk landscape. Variables 4-10 indicate parameters controlling the b-spline functions. These were estimated using 500 samples randomly drawn from the posterior distribution.

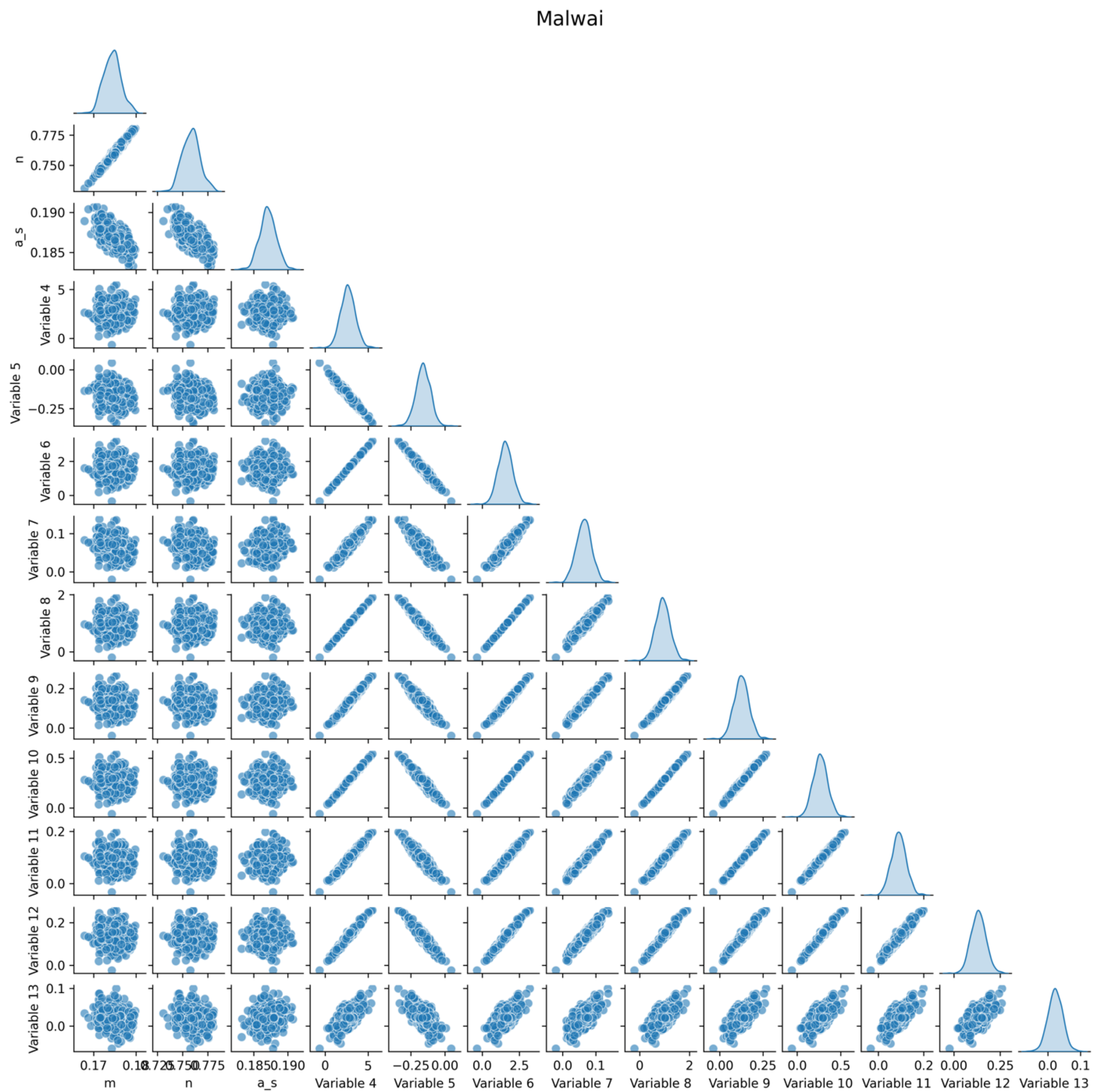

Figure S15 - Pair plots for the Malwai landscape. Variable 4-13 indicate parameters controlling the b-spline functions. These were estimated using 500 samples randomly drawn from the posterior distribution.

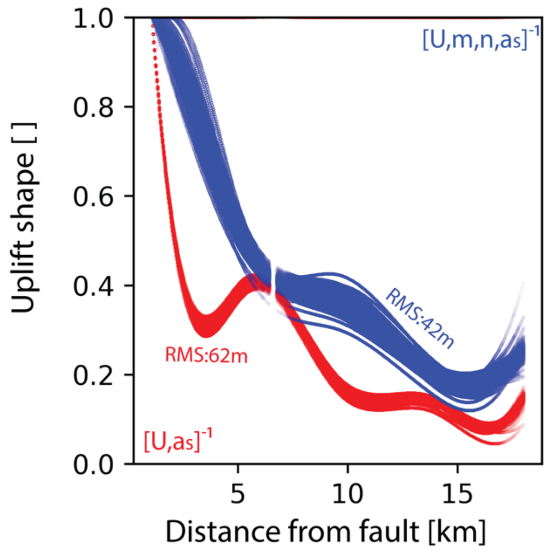

Fig S16 – Comparison of uplift solutions for Wassuk Range for the case the inversion is fixed at m=0.45 and n=1. Colored curve show 500 uplift solutions randomly sampled from our posterior distributions.

	Tethyan Sedimentary Sequence (TTS)	Upper Greater Himalayan Sequence (UGS)	Lesser Himalayan Sequence (LHS)	Lower Greater Himalayan Sequence (LGHS)
Relative erodibility value	0.88 ± 0.40	1.19 ± 0.54	1.01 ± 0.46	0.87 ± 0.39

Table S3 – Best-fitting and standard deviation of relative erodibility values for the Himalayan inversion including the climate effect.

Text S3 – Furter exploration of temporally varying uplift rates

To investigate the impact of variable uplift rates, we modeled 29 landscapes, each initially at steady state under a uniform uplift rate of 1.2 mm/year. We then simulated each landscape over an additional 400K years, during which uplift rates linearly adjusted to final values between 12 and 0.12 mm/year (Fig. S12). This 400K-year period is designed to reflect the fastest changes in uplift rate recorded along Utah's Wasatch Fault (Smith et al., 2024). Throughout this time interval, we retained and inverted 12 landscape snapshots, allowing us to assess the temporal variation in landscape response. The results we present are averaged from these 12 landscape analyses.

Our inversion reveals that greater contrasts in uplift rates lead to pronounced deviations from the imposed landscape properties. For instance, a tenfold increase in uplift rate results in RMS values ranging from 3 to 7 times larger than the baseline (Fig. S12). Notably, landscapes experiencing an increase in uplift rate exhibit RMS values approximately twice as large as those undergoing a decrease (Fig. S12A). This difference likely stems from the landscape's delayed response in adjusting to reduced rock removal at lower uplift rates. The erodibility of the rock affects this asymmetry, with higher erodibility potentially reversing the trend. Despite less precision with significant uplift increases, the inversion still accurately captures the uplift pattern, albeit with a slight, consistent deviation from the imposed configuration (Figs. S12D1 & S12D2).

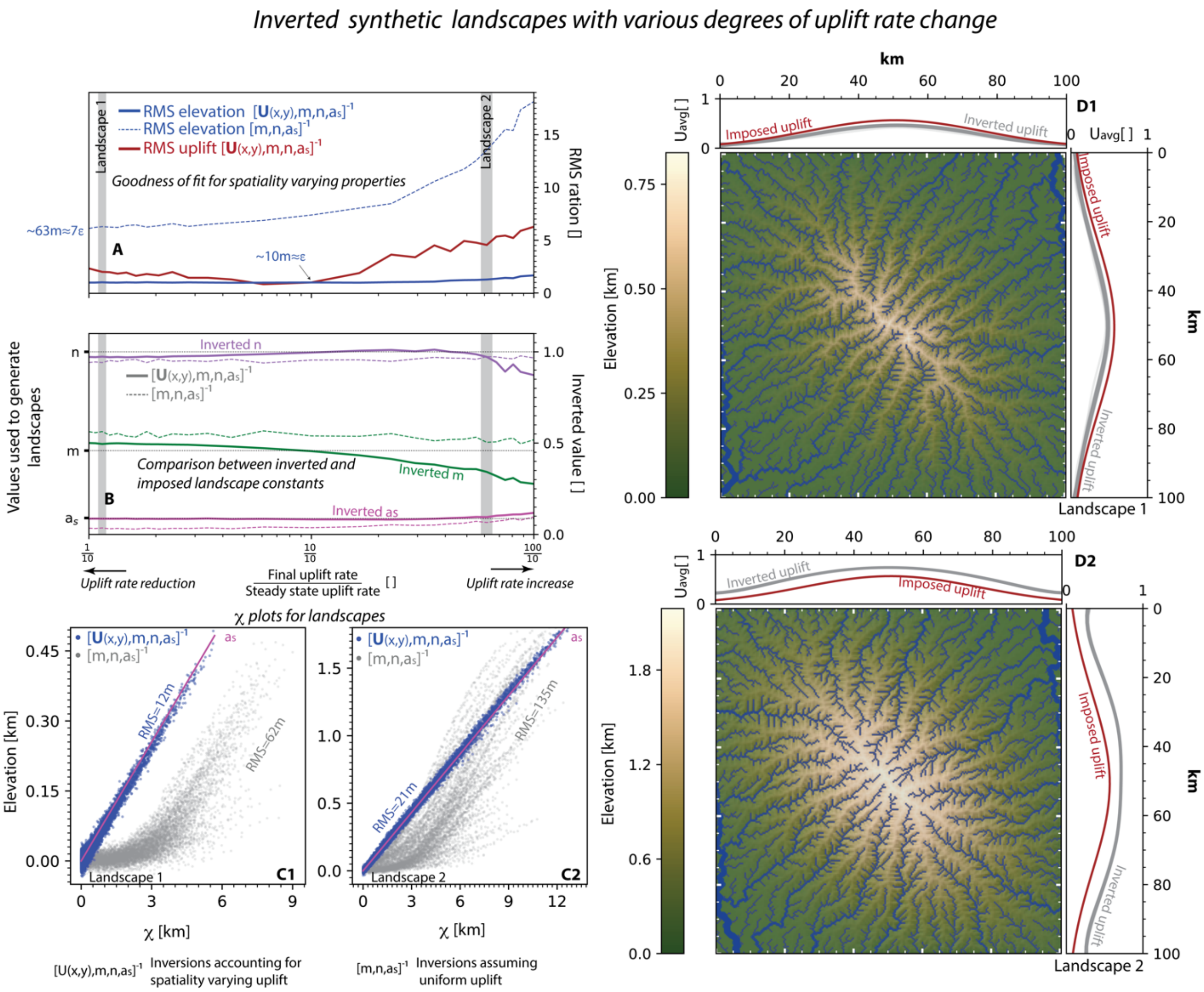

Figure S17 – Inverted synthetic landscapes with varying degrees of temporal changes in imposed tectonic uplift rate. Panels A and B show comparison between imposed and recovered landscape properties for inversions of 50 synthetic landscapes, each characterized by a distinct final uplift rate value employed in simulating the landscape. Values shown in panels A and B are averaged for 12 snapshots of the landscape during the 400K years over which the change in rate occurred. Panels C & D show the results for the last time step of the tectonic rate change. See Fig. 2 for complete figure description.

Text S4 – Furter exploration of temporally varying uplift shape

We modeled 48 landscapes that initially reach a topographic steady state, featuring an uplifting domain along the southern edge of the model (Table S1; Fig. S1). We then reduce uplift rate along the southern edge while commensurably increasing it along the northern edge, causing the mountain range to migrate north (e.g., Fig S13D1). Each landscape is associated with a distinct migration period ranging 120K to 12 M years (Figs. S13 & S1; Table S1). We report the average results for retained 12 snapshots of each landscape intervals during this migration process.

The inversion results in realistic inversion outputs with elevation RMS values only a few meters higher than ε when the timescale of tectonic changes is ≥6 Myr (Figs. S13A, S13B & S13D1). In contrast, faster temporal changes, which build synthetic topography at rate of at least 0.17 $mm \cdot yr^{-1}$ results in inverted uplift showing increasingly larger deviation from imposed uplift (Figs S13A & S13B).

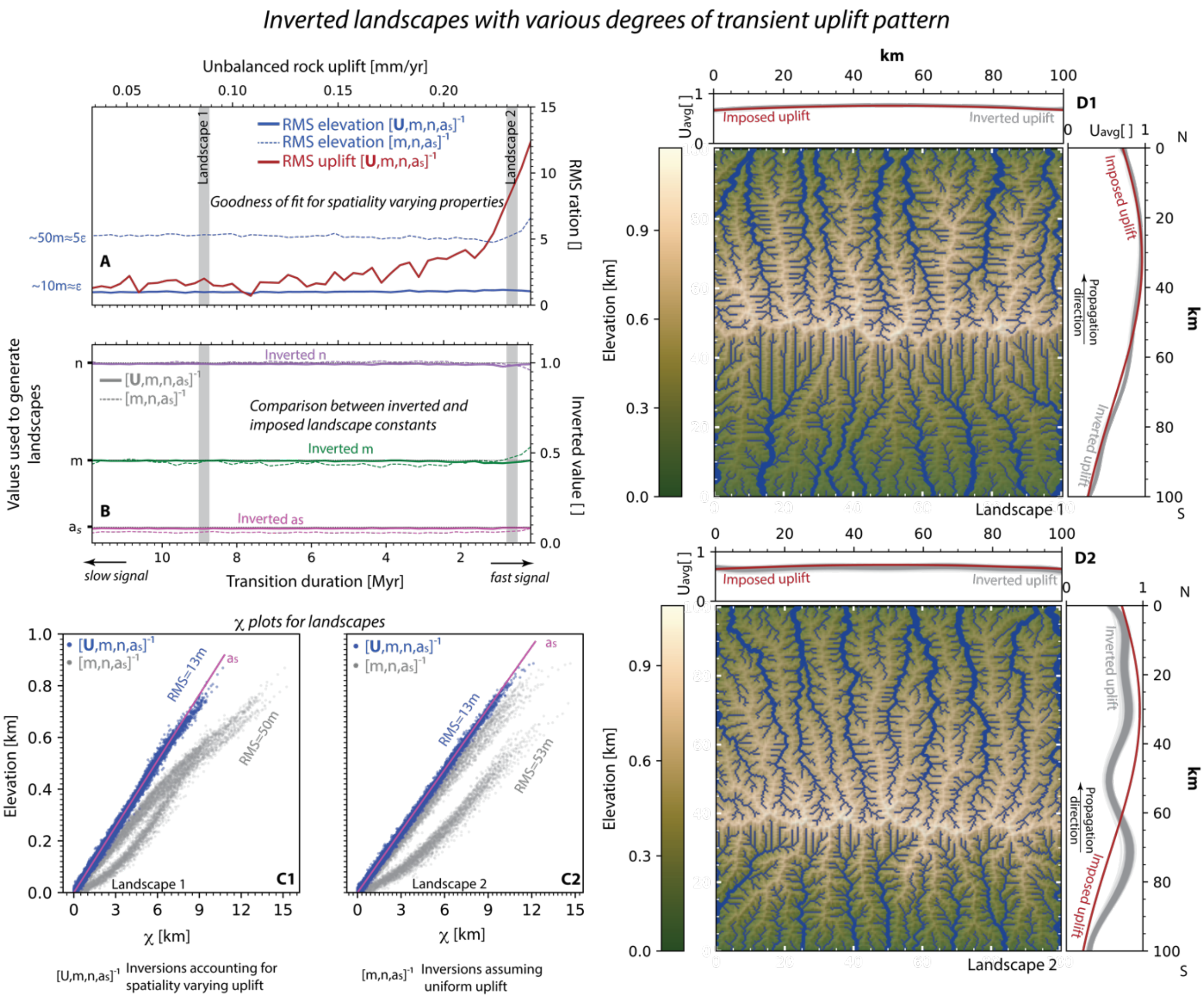

Figure S18 – Inverted synthetic landscapes subject to varying temporal changes in the imposed tectonic uplift pattern. Panels A and B show comparison between imposed and recovered landscape properties for inversions of 50 synthetic landscapes, each characterized by a distinct duration of north migrating uplift signal value. Values shown in panels A&B are averaged for 12 snapshots of the landscape during the migration processes while panels C & D show the results for the last time step of the tectonic migration. See Fig. 2 for complete figure description.

Text S5 – Estimating k_0 and knickpoint travel time

We use our inverted m, n, a_s and previous estimations of u_o $(\mathrm{Table\ S2;\ Ellis\ \&\ Barnes, 2015})$ to retrieve k_0 using $k_0 = \frac{u_0}{a_s^n A_0^m}$. For Lake Malawi and Sandia landscapes, where direct uplift rate estimations are unavailable, we follow $\mathrm{Ellis\ \&\ Barnes\ (2015)}$ and estimate the minimum uplift rate using timing of fault initiation and a linear scaling relationship between fault displacement and length (Schlische et al., 1996)

Lake Malawi and the Kipengere Range, known as the Livingstone Mountains, have formed due to flexural-isostatic rebound in response to localized extension at the southern end of the East African Rift. High-resolution seismic imaging of sediments deposited in the northern basin of Lake Malawi along the ~80km long Livingstone Fault, the focus of our analysis, suggests a fault displacement (throw) of between 6.6 and 7.4 km. (Accardo et al., 2018). Apatite thermochronology along the Livingstone fault system indicates that regional cooling, associated with the onset of Cenozoic rifting, started approximately 23 million years ago (Mortimer et al., 2016). This results in uplift rate of 0.12 $mm \cdot yr^{-1}$.

The Sandia fault delineates the steep western face of the Sandia Mountains and marks the eastern boundary of the Albuquerque basin part of the Rio Grande Rift. Apatite fission track (AFT) and (U-Th)/He data from the Sandia Mountains indicate fault activity and rapid cooling 22-17Ma (House et al., 2003). Using fault length of 100km (McCalpin & Harrison, 2006) we estimate minimum uplift rate of 0.14 $mm \cdot yr^{-1}$.

Finally, we use equation (3) to compute knickpoint travel time from the base level(Fig. S13). We would like to note that we calculate the drainage pattern assuming a uniform precipitation rate of $1\ m \cdot yr^{-1}$, which is generally a reasonable value except for the Sandia and Wassuk regions where rainfall is lower. However, we disregard this effect as these landscapes are in a steady state, and lowering the uniform precipitation rate would reduce A_0, leading to even faster travel times.

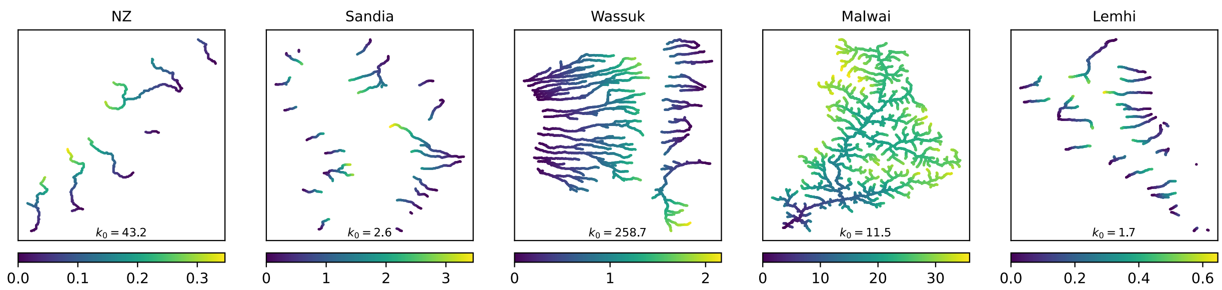

Fig S19 – Travel time in million years for the five natural landscapes used in the study. Colormap shows travel time from river base. k_0 shows 10^{-6} erodibility values.

Text S6 – Estimating deflection wavelength

Theory

The deflection of a broken thin elastic plate overlying a viscous half space subject to kilometer long offset is expressed as (Nadai, 1963):

$$1.\quad w(x) = w_0 \cdot \exp\left(-\frac{x}{\alpha_b}\right) \cdot \cos\left(\frac{x}{\alpha_b}\right)$$

Where w_0 is the deflection at the fault axis, x distance from the fault, and α_b is the flexure wavelength:

$$2.\quad \alpha_b = \alpha_0 T_e^{\frac{3}{4}}$$

Where α_0 coefficient linking deflection wavelength and the elastic plate thickness, T_e, and is often expressed as:

$$3.\quad \alpha_0 = \left(\frac{E}{3(\rho_m - \rho_c) \cdot g(1 - v^2)}\right)^{\frac{1}{4}}$$

Where E is Young's modulus, g gravity , v Poission's ration and ρ_m and ρ_c are the densities of the viscous layers and elastic layers, respectively.

Estimating α_0 from our inverted 1D uplift profile

To estimate α_b for each landscape we used our inverted 1D uplift profiles and fitted it with a simplified version of equation (1): $u(x) = w_o \cdot e^{\frac{-x}{\alpha_b}}$ (Fig. S15). We then fitted equation (2) and found $\alpha_0 = 1.2\ km^{1/4}$ (Fig. S16). Assuming $E = 30GPa$, $v = 0.25$ and $\rho_m - \rho_c = 300 \frac{kg}{m^3}$ yield $\alpha_0 = 43.6\ km^{1/4}$. Lastly, we note that we utilized Python's scipy module relying on non-linear least squares to fit the data shown in this section (Vugrin et al., 2007).

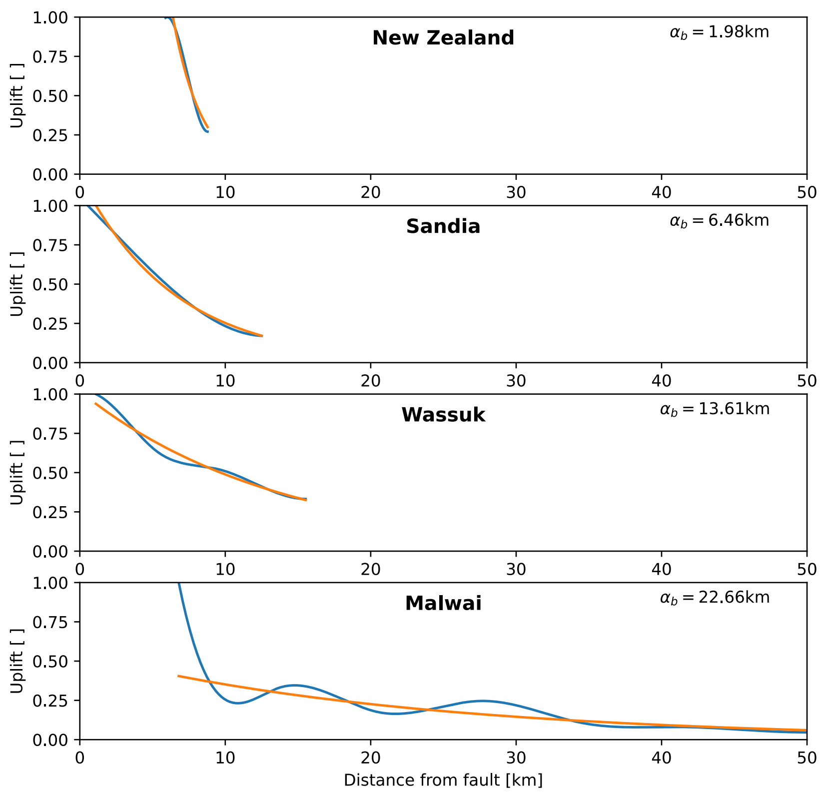

Fig S20 – Fitted wavelength for landscapes. Blue curves show best inverted uplift pattern for landscapes. Orange lines show $a \cdot e^{\frac{-x}{b}}$ curves fitted to uplift solutions.

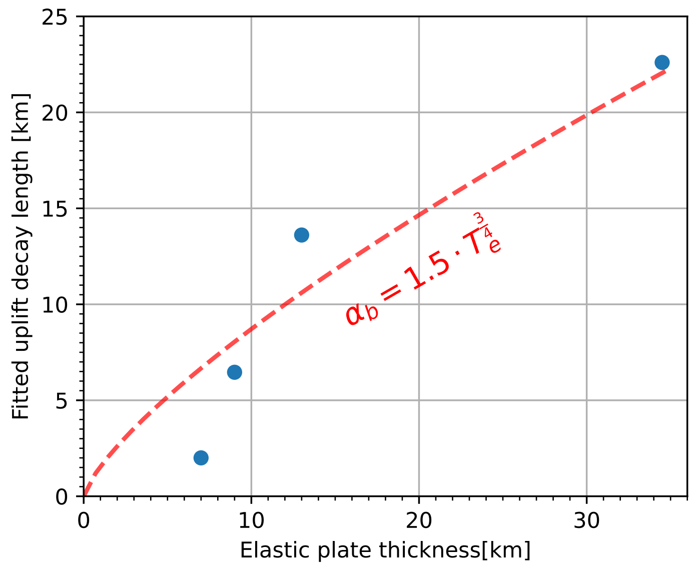

Fig S21 – Fitted equation (2) for landscapes. Blue dots show properties of landscape we used and red curve show fitted line.